

# Depletion of CD206<sup>+</sup> tumour macrophages by mUNO targeted nanoconjugate inhibits tumourigenesis and dissemination in triple negative breast cancer

**Anni Lepland**

Laboratory of Precision and Nanomedicine, Institute of Biomedicine and Translational Medicine, University of Tartu <https://orcid.org/0000-0002-6448-4847>

**Alessio Malfanti**

Polymer Therapeutics Laboratory, Prince Felipe Research Center

**Uku Haljasorg**

Molecular Pathology Research Group, Institute of Biomedicine and Translational Medicine, University of Tartu <https://orcid.org/0000-0002-1541-6020>

**Eliana Ascitutto**

School of Science and Technology, National University of San Martin (UNSAM) ICIFI and CONICET.

**Monica Pickholz**

Departamento de Física, Facultad de Ciencias Exactas y Naturales, Universidad de Buenos Aires; Instituto de Física de Buenos Aires (IFIBA), CONICET-Universidad de Buenos Aires

**Mauro Bringas**

Departamento de Química Inorgánica, Analítica y Química Física, Facultad de Ciencias Exactas y Naturales, Universidad de Buenos Aires; Fundación Instituto L

**Snežana Đorđević**

Polymer Therapeutics Laboratory, Prince Felipe Research Center

**Liis Salumäe**

Tartu University Hospital, Pathology department

**Pärt Peterson**

Molecular Pathology Research Group, Institute of Biomedicine and Translational Medicine, University of Tartu <https://orcid.org/0000-0001-6755-791X>

**Tambet Teesalu**

Laboratory of Precision and Nanomedicine, Institute of Biomedicine and Translational Medicine, University of Tartu; Centre for Nanomedicine and Department of Cell, Molecular and Developmental Biolog

**María Vicent**

Polymer Therapeutics Laboratory, Prince Felipe Research Center <https://orcid.org/0000-0001-7771-3373>

**Pablo Scodeller** (✉ [pablo.david.scodeller@ut.ee](mailto:pablo.david.scodeller@ut.ee))

Laboratory of Precision and Nanomedicine, Institute of Biomedicine and Translational Medicine,  
University of Tartu

---

## Article

**Keywords:** triple negative breast cancer, M2-skewed tumour-associated macrophages, CD206+ macrophages

**Posted Date:** August 24th, 2021

**DOI:** <https://doi.org/10.21203/rs.3.rs-839856/v1>

**License:**  This work is licensed under a Creative Commons Attribution 4.0 International License.

[Read Full License](#)

---

# Abstract

Chemotherapy is the standard of care for patients with triple negative breast cancer (TNBC), an aggressive breast cancer subtype with a poor prognosis. In many solid tumours, M2-skewed tumour-associated macrophages (TAMs) are known to promote progression, immunosuppression, relapse, and dissemination of the malignant disease. Although TAM depletion has been explored as an anticancer strategy, the currently available TAM depleting compounds suffer from poor efficacy and dose-limiting side effects.

Here, we develop of a novel TAM-depleting agent that specifically targets CD206<sup>+</sup> macrophages and show that it is efficacious as an anti-TNBC agent and well tolerated. This new TAM-depleting compound, called "OximUNO", is a star-shaped polyglutamate decorated with the CD206-targeting peptide mUNO and carrying doxorubicin through a pH-responsive linker. In the orthotopic and experimental metastases of TNBC, fluorescent reporter mUNO-guided polyglutamate construct homed to CD206<sup>+</sup> macrophages in the primary cancer lesions and at the sites of metastases. OximUNO displayed enhanced cytotoxicity towards primary M2 macrophages in vitro and exhibited no acute liver or kidney toxicity in vivo. In TNBC mouse models, OximUNO reduced the progression of primary breast cancer lesions and metastatic dissemination of malignant cells. Treatment with OximUNO had an immunomodulatory effect on the tumour microenvironment: besides reducing the number of CD206<sup>+</sup> TAMs, it resulted in increased ratio of the CD8/FOXP3 expression. These studies suggest the potential utility of OximUNO based CD206<sup>+</sup> TAM depletion strategies for the treatment of TNBC, and possibly, other types of solid tumours.

## Introduction

Triple negative breast cancer (TNBC), defined by the lack of the expression of the oestrogen receptor (ER), progesterone receptor (PR), and a human epidermal growth factor receptor 2 (HER2)<sup>1,2</sup>, is an aggressive breast cancer subtype with poor prognosis<sup>3</sup> that comprises up to 20% of all breast cancer cases<sup>3,4</sup>. Interfering with immune checkpoints signalling, e.g. through the modulation of programmed cell death 1 (PD-1) and its ligand (PD-L1), represents an alternative treatment strategy for several cancers and is currently being employed in combination with chemotherapy as a neoadjuvant or adjuvant treatment<sup>5-8</sup>. The U.S. Food and Drug Administration (FDA) recently granted accelerated approval for a combination of a PD-L1 blocking antibody (atezolizumab, Tecentriq®) and nab-paclitaxel (Abraxane®)<sup>9</sup> as a first-line treatment for unresectable locally advanced or metastatic TNBC<sup>10</sup>. Although clinical results have been promising, this treatment approach suffers from significant obstacles, including the problematic identification and heterogeneity of PD-L1 expression in patients<sup>11</sup>, the limited applicability to PD-L1 positive TNBC patients (only 20–42% of cases)<sup>12,13</sup>, and the induction of severe side effects (e.g., neutropenia, peripheral neuropathy, and colitis)<sup>10,14,15</sup>. Other immune checkpoint inhibitors (ICIs), including the cytotoxic T lymphocyte-associated antigen 4 (CTLA-4) blockers ipilimumab and tremelimumab, are currently under evaluation for TNBC treatment in combination with other drugs (clinical trial identifiers: NCT03606967, NCT02983045), however, anti-CTLA-4 treatments also induce

severe side effects such as endocrinopathies, myopathy, enterocolitis, and hepatitis<sup>16–19</sup>, which narrow their use. Overall, the limited success of alternative treatment options for TNBC has maintained chemotherapy as the standard of care for most patients<sup>20</sup>.

The anthracycline doxorubicin (DOX), which presents high off-target effects such as cardiotoxicity<sup>21,22</sup>, represents a frequently employed chemotherapeutic for TNBC; however, DOX treatment can lead to disease relapse and favours metastasis<sup>23</sup>. M2 (anti-inflammatory)-skewed tumour-associated macrophages (TAMs)<sup>24</sup> found in both primary and metastatic tumour lesions mediate both these events<sup>25</sup>. Furthermore, TAMs represent the main executioners of tumour progression, immunosuppression and invasion<sup>24–29</sup>, and their presence correlates with inadequate therapeutic response and poor prognosis<sup>25</sup>. Recent efforts have focused on TAM elimination, and several current ongoing clinical trials are evaluating TAM depletion in combination with treatments such as ICI<sup>30</sup>. The current clinical-stage gold standard for TAM depletion relies on agents that block colony stimulating factor 1 (CSF1) or its receptor CSF1R, such as the small molecule CSF1R inhibitor PLX3397<sup>31</sup>; however microglia also expresses CSF1R<sup>32</sup>, the inhibition of CSF1R with PLX5622 also impacts M1 macrophages<sup>33</sup> and with PLX3397 cause oedema<sup>34</sup>. Clinical data suggests that anti-CSF1R antibodies induce a modest effect<sup>35,36</sup> and cause severe side effects that include haematological toxicities<sup>35</sup> and hepatotoxicity due to Kupfer cells targeting<sup>35,36</sup>. Overall, these findings highlight the overwhelming need for new TAM-depleting strategies.

The mannose receptor (CD206/MRC1) is expressed by perivascular TAMs associated with disease relapse and therapeutic resistance<sup>24</sup> and also on metastasis-associated macrophages<sup>37</sup>. Perivascular TAMs use CD206 to navigate the surrounding collagen-dense stroma<sup>38</sup>, which favours tumour progression<sup>39,40</sup>.

Here, we report for the first time the effects of depleting the CD206<sup>+</sup> subpopulation of TAMs in the mouse models of metastatic TNBC. To target the CD206<sup>+</sup> TAMs, we took advantage of a CD206-binding peptide to precisely guide the delivery of a cytotoxic compound. The mUNO peptide (sequence: CSPGAK) targets a CD206 site that differs from the mannose-binding site and displays low accumulation in the liver<sup>41–44</sup>. We decorated a novel, highly negatively charged polymeric carrier comprising a three-pronged polyglutamate with a defined nanometre-size hydrodynamic radius (star-shaped polyglutamate or St-PGA) with mUNO to function as a targeted delivery platform for a conjugated chemotherapeutic agent (DOX). St-PGA-DOX-mUNO, referred to as OximUNO, efficiently depleted CD206<sup>+</sup> TAMs, relieved immunosuppression in the tumour microenvironment (TME) and had a metastasis/tumour growth-limiting activity. Overall, our findings support OximUNO as an alternative to current clinical-stage TAM depletion strategies.

## Results

# The design and structural modelling of St-PGA-OG-mUNO

To characterise and explore the function of OximUNO, we first developed an mUNO-targeted St-PGA labelled with the fluorescent dye Oregon Green (OG) (referred to as St-PGA-OG-mUNO) (Fig. 1A, Scheme 1). We conjugated OG to St-PGA through an amide linker to allow in vitro or in vivo tracking, and we coupled mUNO through a disulphide bond formed between free cysteine of mUNO and a pyridyldithiol linker on St-PGA. We have previously demonstrated that mUNO conjugated to polymeric nanostructures through the thiol group of its cysteine preserves CD206 binding<sup>42</sup>. To evaluate the structure and dye loading, we analysed St-PGA-OG-mUNO and St-PGA-OG using nuclear magnetic resonance (NMR) and UV-Vis analyses (Fig. S1). Dynamic light scattering (DLS) analysis demonstrated that St-PGA-OG-mUNO and St-PGA-OG displayed similar hydrodynamic diameter of 6.8 and 5.9 nm, respectively (Fig. 1B, C), while both nanoconjugates exhibited highly negative charges (-42 mV and -48 mV, respectively) as shown by Zeta potential analysis (Fig. 1B); an expected result given the glutamic acid nature of the polymer carrier. Analysis of mUNO loading (Fig. 2B) indicated the presence of approximately seven mUNO peptides in St-PGA-mUNO nanoconjugate, providing for desired multivalency.

We next assessed the structure of unlabelled and untargeted St-PGA in water using molecular dynamics (MD) simulations to access information at the atomic scale. We assumed an initial helical conformation for the three PGA chains. The studied system consisted of a fully hydrated St-PGA and the Na<sup>+</sup> counterions (~ 920 000 atoms) and was built after an initial minimisation in vacuum conditions. We simulated 50 ns of the entire St-PGA macromolecule and Fig. 1D displays a snapshot corresponding to the last step of the simulation. We averaged the gyration radius over the last 25 ns of the simulation run, which provided a value of  $5.6 \pm 0.3$  nm, which lies in the same order of magnitude as the results from DLS analysis and suggests a lack of aggregation of both St-PGA-OG-mUNO and St-PGA-OG in PBS. The video simulation (Video S1) suggests that the three PGA chains remain in an extended conformation throughout the simulation and do not interact, suggesting that the mUNO peptides linked to St-PGA will not interfere with each other.

To investigate if mUNO can engage with its receptor CD206 when grafted onto St-PGA, we modelled the structure and mobility of St-PGA-mUNO using computational analysis. To attain a computationally feasible system, we simulated only single branches of St-PGA-mUNO. We placed three equidistant mUNO peptides on a PGA single branch and fully solvated the system. We observed that three mUNO peptides remained exposed to the solution available for receptor binding (Fig. 1E). The rotation of mUNO around PGA, tracked by the angle formed by an aromatic carbon of mUNO's proline (Fig. S2, green sphere), a nitrogen of the pyridyldithiol linker (Fig. S2, blue sphere) and an aromatic carbon of the glutamic acid (Fig. S2, light blue sphere) revealed angles between 50° and 180° (Fig. 1F), in line with the availability of the mUNO peptides to interact with their receptor<sup>43</sup>. Comparisons with an undecorated PGA branch demonstrated the minimal alterations of secondary structure dynamics in the presence of mUNO peptides; turning alpha helices (green, Fig. 1G) into random coils (brown, Fig. 2C) only at the regions

where they are placed; however, the PGA chain structure remained mainly helical except in the middle, where a slight kink formed (Fig. 1G).

Altogether, St-PGA-OG-mUNO and St-PGA-OG nanoconjugates display similar sizes by DLS, are highly negatively charged, and according to the simulations display their three arms in an extended open structure. Our simulation analyses demonstrated that mUNO peptides have a minimal effect on the PGA structure and that peptides rotate around the PGA chain with considerable freedom. Overall, these findings suggest that the St-PGA-mUNO is a suitable platform for CD206 targeting.

## **St-PGA-OG-mUNO targets CD206<sup>+</sup> TAMs and displays low accumulation in the liver**

We next evaluated the potential of the St-PGA-OG-mUNO nanoconjugate to target CD206<sup>+</sup> TAMs in the TNBC models – an orthotopic TNBC model and an experimental metastases of TNBC model induced by intravenously (i.v.) injecting 4T1 cells. We administered intraperitoneally (i.p.) St-PGA-OG-mUNO or St-PGA-OG, allowed circulation for 6 h, and then analysed tumour homing using confocal fluorescence microscopy. In the orthotopic TNBC, we observed a high colocalisation of OG/CD206 (Fig. 2A, yellow signal) with St-PGA-OG-mUNO but a much lower colocalisation of OG/CD206 with non-targeted St-PGA-OG (Fig. 2B) (0.57 and 0.21, respectively (Fig. 2I)). We observed a low level of accumulation of St-PGA-OG-mUNO or St-PGA-OG in the liver (Fig. S2A, B), which correlates with low CD206 expression in hepatic tissue compared to the high CD206 expression in TAMs<sup>41</sup>. Importantly, we did not detect homing to M1 macrophages (CD86<sup>+</sup>) or dendritic cells (CD11c<sup>+</sup>, DCs) with St-PGA-OG-mUNO (Fig. 2C, E) or with St-PGA-OG (Fig. 2D, F). In the experimental metastases of TNBC, most of the cellular signal of St-PGA-OG-mUNO was associated with CD206<sup>+</sup> TAMs (Fig. 2G, yellow signal), compared to St-PGA-OG (Fig. 2H) (OG/CD206 colocalisation 0.42 and 0.14, respectively, Fig. 2N). Also in this model, we observed no colocalisation between OG and CD86 (M1 macrophages) (Fig. 2I, J) or OG and CD11c (DCs) (Fig. 2K, L) and the accumulation of St-PGA-OG-mUNO or St-PGA-OG was low in the liver (Fig. S4).

One of the rationales behind the design of OximUNO was to increase mUNO targeting through avidity and an increased half-life. To evaluate these aspects, we compared the homing of St-PGA-OG-mUNO with a monomeric, carboxyfluorescein-labelled mUNO peptide (FAM-mUNO). We discovered that St-PGA-OG-mUNO (Fig. S5A) displayed significantly higher OG/CD206 colocalisation than FAM/CD206 in the FAM-mUNO (Fig. S5B) at 6 h timepoint (0.74 vs. 0.21, respectively (Fig. 2O)). Additionally, we found that the OG/FAM mean signal per CD206<sup>+</sup> cell was 5x higher for St-PGA-OG-mUNO compared to FAM-mUNO (Fig. 2P). These findings demonstrate that conjugating mUNO to the St-PGA backbone greatly improved receptor binding.

The plasma half-life analysis for i.p. administered St-PGA-OG-mUNO revealed a 4.5 h half-life (Fig. 2Q), a value 2.4x longer than the value reported for the i.p. administration of FAM-mUNO in our previous study<sup>42</sup>. Overall, this finding indicates that conjugating the mUNO peptide to St-PGA increased its plasma half-life, a desirable feature that will improve in vivo ligand targeting.

Administration of a higher dose of both nanoconjugates (0.82 mg/0.5mL St-PGA-OG-mUNO and 0.7 mg/0.5mL St-PGA-OG) resulted in high CD206<sup>+</sup> TAM targeting (Fig. S6A) albeit at higher accumulation in the liver (Fig. S6C). For this reason, we decided to use the lower nanoconjugate doses (0.41 mg/0.5mL and 0.35 mg/0.5mL) for subsequent studies.

Overall, we demonstrated that St-PGA-OG-mUNO, homes to the CD206<sup>+</sup> TAMs in both orthotopic and experimental metastases of TNBC with low accumulation in the liver. We also established that St-PGA-OG-mUNO does not target M1 macrophages or DCs in the tumour, thereby providing evidence of high specificity for CD206<sup>+</sup> TAMs.

## OximUNO enhances the cytotoxicity of DOX on M2 macrophages in vitro

St-PGA displays a large surface with multiple sites available for the conjugation of pro-apoptotic or cytotoxic cargo via bioresponsive polymer-drug linkers<sup>45,46</sup>. To selectively deplete CD206<sup>+</sup> TAMs, we conjugated an apoptotic agent (DOX) to St-PGA-mUNO to form St-PGA-DOX-mUNO, more simply, OximUNO (Fig. 3A, Scheme S2). We conjugated DOX to St-PGA-mUNO through a hydrazone bond<sup>45</sup> to allow for site-specific drug release in the acidic milieu of the endosomes/lysosomes<sup>45,47</sup>. To evaluate the effect of mUNO targeting, we included St-PGA-DOX as an untargeted control. We employed <sup>1</sup>H NMR and UV-Vis analyses to evaluate the chemical identity of these nanoconjugates (Fig. S7A).

OximUNO displayed DOX and mUNO loadings of ~ 10% and ~ 4% in weight, respectively, corresponding to around four DOX and seven mUNO molecules for every OximUNO. OximUNO exhibited a size of ~ 40 nm and a highly negative surface charge of -40 mV (Fig. 3B, C). We obtained similar DOX loading, size by DLS, and surface charge values for St-PGA-DOX (Fig. 3B, C). Upon cellular internalisation, DOX release from OximUNO is expected to occur due to the presence of the pH-sensitive hydrazone linker and the intrinsic biodegradability of St-PGA by lysosomal protease cathepsin B<sup>48</sup>. Hence, we studied DOX release kinetics from OximUNO in the presence of acidic pH (pH 5) and cathepsin B using liquid chromatography-mass spectrometry (LC-MS, Fig. S8). As we aimed to administer OximUNO i.p., we also assessed DOX release in the intraperitoneal fluid (i.p. fluid) (Fig. 3D). At pH 5, we observed a sustained DOX release profile in the first 8 h (reaching a plateau at 15%), thereby demonstrating the suitability for endo-lysosomal drug delivery. DOX release in the presence of cathepsin B displayed comparable values in the first 8 h (~ 13%), followed by a plateau and a reduced rate in the following hours (~ 13% cumulative release at 72 h). Importantly, OximUNO exhibited negligible drug release in both physiological conditions evaluated (PBS and i.p. fluid) (Fig. 3D).

We next evaluated the in vitro cytotoxicity of OximUNO and St-PGA-DOX in primary human blood monocyte-derived M2 and M1 macrophages. To emulate the in vivo concentration that provided the optimal CD206<sup>+</sup> TAMs targeting with minimal accumulation in the liver (30 µM in OG), we tested the conjugates at 33µM in DOX loading. We used an incubation time of 15 min to imitate the in vivo contact time of a circulating nanoconjugate with tissue macrophages. Under these conditions, free DOX was not

toxic to M2 or M1 macrophages (Fig. 3E, purple bar). In contrast, OximUNO displayed significantly higher toxicity against M2 macrophages than DOX (52%) and St-PGA-DOX (33%) (Fig. 3E). On M1 macrophages, OximUNO exhibited 2x less toxicity than St-PGA-DOX. Interestingly, St-PGA-DOX showed higher toxicity in M1 than in M2 macrophages (Fig. 3E, blue bar), possibly because M1 macrophages display greater phagocytic activity than M2 macrophages<sup>49,50</sup>, which might also explain the 60% cell viability following OximUNO treatment on M1 macrophages (Fig. 3E, red bar). We observed a very similar trend using a higher concentration of DOX (100µM); however, free DOX displayed notable toxicity on M2 macrophages at this higher concentration (Fig. 3E). These results provide evidence that OximUNO displayed increased toxicity towards M2 macrophages when compared to St-PGA-DOX or DOX alone. While OximUNO induced a degree of in vitro toxicity towards M1 macrophages, our homing studies revealed that in vivo, St-PGA-OG-mUNO did not target M1 macrophages (Fig. 2C, I).

We also evaluated the hepatic and renal safety profile of OximUNO by analysing creatinine (Crea) and alanine aminotransferase (ALAT) levels after its i.p. administration in healthy mice. We saw no increase in Crea or ALAT (Fig. 3F) following OximUNO administration compared to the values reported in the literature<sup>51</sup> or the reference values for the female Balb/c reported in the Mouse Phenome Database by The Jackson Laboratory<sup>52</sup> or Charles River facilities<sup>53</sup>.

In summary, the conjugation of mUNO and DOX to the St-PGA backbone to yield OximUNO, enhanced the in vitro efficacy of DOX towards M2 macrophages with no in vivo renal or hepatic toxicity observed.

## **OximUNO monotherapy in the orthotopic TNBC depletes CD206<sup>+</sup> TAMs, inhibits tumour progression and attenuates immunosuppression**

The findings of the in vivo homing and in vitro cytotoxicity studies supported the subsequent evaluation of OximUNO in the orthotopic TNBC. When induced tumours reached 25 mm<sup>3</sup>, we treated mice with i.p. injections of OximUNO, St-PGA-DOX, or DOX, at 2mg/kg of DOX every other day for 18 days. Encouragingly, OximUNO treatment significantly reduced primary tumour volume growth kinetics (Fig. 4A, red line) compared to DOX, St-PGA-DOX, and PBS. Furthermore, only the OximUNO treatment significantly reduced the final tumour weight (Fig. 4B) compared to the untreated group. We assigned this encouraging therapeutic effect to mUNO-mediated targeting as animals treated with the untargeted St-PGA-DOX showed tumour volumes (Fig. 4A, blue line) similar to the PBS group (Fig. 4A, black line). Notably, OximUNO treatment had no effect on bodyweights of the mice whereas treatment with DOX induced a significant decrease in bodyweights of mice starting from day 21 post inoculation (p.i.) until the end of the treatment (Fig. 5C). Histological analysis of the lungs (healthy lung H&E shown in Fig. S9) revealed that OximUNO also influenced pulmonary metastases (Fig. 4D), as it elicited the highest reduction in the metastatic lung area and the number of nodules (p = 0.06 vs. PBS for both). Histological analysis revealed no cardiotoxicity in any of the groups (Fig. S10). Tumour tissue section immunofluorescence (IF) revealed that only OximUNO significantly reduced the CD206 expression (assigned to CD206<sup>+</sup> TAMs),

compared to PBS (Fig. 4G, J). Interestingly, treatment with DOX upregulated the expression of CD206 (Fig. 4G, J), which agrees with previous reports on chemotherapy increasing the amount of CD206<sup>+</sup> TAMs<sup>24</sup>. Notably, only OximUNO significantly increased the expression of CD8 a marker of cytotoxic T cells (CTLs) compared to PBS and DOX (Fig. 4H, K). Unexpectedly, St-PGA-DOX treatment resulted in an increase in the expression of FOXP3, a marker for regulatory T cells (Tregs) (Fig. 4I, L). Analysis of the CD8/FOXP3 expression ratio revealed that OximUNO treatment resulted in a 5-fold increase compared to St-PGA-DOX or DOX alone (Fig. 4M), suggesting that OximUNO stimulated a shift in the immune landscape towards more immunostimulatory.

By targeting DOX to CD206<sup>+</sup> TAMs via OximUNO treatment, we increased the efficacy and reduced the toxicity of DOX in the orthotopic TNBC. Our results also suggested that the therapeutic effect of OximUNO was mediated by the depletion of CD206<sup>+</sup> TAMs which in turn elicited an immunostimulatory shift.

## **OximUNO monotherapy in the experimental metastases of TNBC reduces tumour burden and CD206<sup>+</sup> TAMs**

We next evaluated the effect of OximUNO on the experimental metastases of TNBC using GFP-labelled 4T1 cells. We treated mice every other day via i.p. injections of OximUNO, St-PGA-DOX, or DOX, starting from day four p.i. and sacrificed on day 18 p.i. Analysis of whole lung fluorescence in the green channel revealed that OximUNO treatment induced the lowest GFP fluorescence, indicating a reduced amount of cancer cells inside the lungs (Fig. 5A), which can also be seen from the representative macroscopic images (Fig. 5B). Confocal fluorescence microscopy of lungs confirmed the trend we observed with whole lung fluorescence, showing fewer GFP fluorescent nodules in the OximUNO-treated group (Fig. 5C). Furthermore, histological analysis of lungs displayed the least pulmonary nodules for OximUNO-treated mice (Fig. 5D). Mice treated with the untargeted St-PGA-DOX and free DOX showed significant decrease in bodyweights, resulting in 19% (Fig. 5D, blue line) or 17% total loss (Fig. 5E, purple line), respectively. Encouragingly, OximUNO-treated mice exhibited less bodyweight loss (Fig. 5E, red line), better fur appearance, and less ataxia by the end of treatment. We used flow cytometry (FC) to analyse the effect of the different treatments on the immune cell populations in whole lungs, which established that OximUNO monotherapy significantly lowered the percentage of M2 TAMs (CD206<sup>+</sup>) (Fig. 5F), but did not significantly impact M1 TAMs, CTLs, or Tregs (Fig. 5F-I). We observed the same trend when we expressed these populations as total cell counts (Fig. S11-S13). FC analysis informed us of the immune status of the whole lung but not specifically of the TME. To specifically characterise the immune landscape of the TME, we next analysed the expression of markers for TAMs, CTLs, and Tregs in pulmonary nodules using IF. Analysis revealed significantly lower CD206 expression for the OximUNO-treated group than PBS (Fig. 5J, N), providing evidence for the robust reduction in the number of CD206<sup>+</sup> TAMs in the TME. Importantly and similarly to the OximUNO treatment in the orthotopic TNBC, OximUNO elicited the highest expression of CD8 (Fig. 5K, O). OximUNO and St-PGA-DOX treated lungs demonstrated significantly lower FOXP3 expression compared with PBS and DOX (Fig. 5L, P), and a 2.6x or 2.8x higher CD8/FOXP3

expression ratio for OximUNO when compared with St-PGA-DOX and DOX, respectively, and 6.9x higher than with PBS (Fig. 5M). Therefore, our IF analysis in the tumour nodules suggested that OximUNO triggered a shift in the immune profile of the TME towards more immunostimulatory.

By targeting DOX to CD206<sup>+</sup> TAMs in the experimental metastases of TNBC, we increased the efficacy and reduced the toxicity of DOX, as OximUNO treatment led to the presence of fewer pulmonary tumour lesions and less bodyweight loss when compared to the treatment with untargeted St-PGA-DOX and free DOX. Our results suggest that the observed therapeutic effect derived from the CD206<sup>+</sup> TAM depletion, which elicited an immunological shift in the TME.

## Discussion

To date, TNBC remains an aggressive breast cancer subtype<sup>3</sup> with few treatment options, conventional chemotherapy still remaining as the standard of care<sup>20</sup>. ICIs for TNBC have provided only modest improvements in complete response and progression free survival and only in a small subset of TNBC patients<sup>9,12,15,16</sup>. Targeting TAMs can potentiate ICIs and other modalities and, therefore, represents an intense area of study<sup>54–58</sup>. However, TAMs are a diverse population<sup>59–61</sup>, and which TAM subtype to target and how to intervene on it, is still under investigation.

There exist promising TAM-focused interventions under clinical evaluation, such as antibody-mediated depletion of TREM2-expressing TAMs (clinical trial identifier: NCT04691375). Strategies targeting generic TAM markers such as CSF1R and CCR2 have shown limited efficacy and could have severe side effects. Appealing studies have used anti-CD163 antibodies to target TAMs<sup>62</sup> by decorating doxorubicin-carrying liposomes with anti-CD163, to deplete TAMs and potentiate ICIs in melanoma. Folate, a small molecule, is at present in phase III clinical trials (clinical trial identifier: NCT03180307) as a targeting ligand and is now also under study to target TAMs, ever since the folate receptor- $\beta$  was discovered to be upregulated on M2 TAMs<sup>63</sup>. Antibody blockade of Clever-1 on M2 TAMs stimulated an M2 $\diamond$ M1 switch in TNBC models (4T1) and synergised with the PD-1 blockade<sup>64</sup>.

Motivated by the preponderance of the mannose receptor in tumourigenic/metastatic TAMs in breast cancer<sup>65–67</sup>, here, we set out to deplete CD206<sup>+</sup> TAMs in aggressive and metastatic TNBC models and study the consequences on the progression and immunosuppressive state of the tumour.

Several CD206-targeting ligands have been reported. The CD206-binding nanobody developed by Ginderachter et al<sup>68</sup> showed homing to CD206<sup>+</sup> TAMs in in vivo models of lung and breast cancers<sup>68</sup>. Navidea Inc. has engineered a mannosylated compound<sup>69</sup> called Manocept™, which is used in the FDA-approved contrast agent Lymphoseek®. Unfortunately, mannose-based ligands have other binding partners besides CD206, such as CD209 in intestinal and genital tissues<sup>70</sup> and they also can target dendritic cells<sup>71</sup>. Riptide Inc. has designed the peptide known as RP-182 that binds to CD206 but also to RelB, Sirp- $\alpha$  and CD47<sup>72</sup>.

In recent years, we identified and described a short peptide called mUNO (sequence: CSPGAK) that targets mouse<sup>41</sup> and human CD206<sup>43</sup> at a different binding site than mannose on CD206<sup>43</sup>. The peptide was identified from an in vivo screen of a peptide library in mice bearing metastatic breast cancer and was later shown to home to CD206<sup>+</sup> TAMs of other solid tumour models<sup>41,73</sup> and in early-stage models of TNBC<sup>42</sup> with low accumulation in the liver.

We envisioned that conjugating mUNO to the star-shaped polyglutamic acid (St-PGA) would significantly enhance targeting through multivalent presentation (avidity effect) and increase in the plasma half-life<sup>74</sup>.

Compared to synthetic polymers such as N-(2-hydroxypropyl) methacrylamide (HPMA), polypeptide-based nanocarriers show several benefits, which include higher biodegradability, lower immunogenicity and a lack of long term-accumulation (vacuolisation), and the number of polypeptide-based constructs reaching clinical evaluation has significantly increased in the recent years<sup>75-77</sup>. We employed St-PGA-based nanoconjugates that consist of three linear chains (~ 50 glutamic acids each) linked to a central core. Overall, St-PGA is safe, non-toxic and biodegradable, and therefore meets the FDA's approval criteria<sup>78</sup>. A previous screen of PGA structures suggested that larger architectures enhanced plasma half-life and increased bioavailability through a higher hydrodynamic volume that reduces rapid renal clearance<sup>79,80</sup>. An extended plasma half-life is expected to be an advantage when targeting TAMs, which are continuously replenished<sup>81,82</sup>.

Our homing studies showed that St-PGA-OG-mUNO displayed a far greater plasma half-life and specificity to CD206<sup>+</sup> TAMs than free mUNO and avoided CD86<sup>+</sup> M1 TAMs and CD11c<sup>+</sup> DCs, an important fact since M1 TAMs display an anti-tumourigenic activity<sup>25</sup>, and CD11c<sup>+</sup> DCs participate in antigen presentation<sup>83</sup>. In line with these observations, computational analysis indicated that mUNO peptides are available to a receptor and sweep a vast space (130°) around PGA. Altogether this data demonstrates the benefit of conjugating mUNO to the St-PGA polymer backbone and represents the first report on peptide-guided precision delivery using the St-PGA platform.

Drug release studies showed that only 15% of DOX was released from OximUNO. These results agree with our previous studies<sup>45,47</sup> but also suggest room for improvement, by using payloads that do not require linker cleavage, such as photosensitizers used for photodynamic therapy<sup>84-86</sup>. To explain why no further release was observed in the presence of Cathepsin B we hypothesise that the nanoconjugate conformation slows down the proteolytic degradation<sup>79</sup>.

Our in vivo efficacy studies showed that, strikingly, the sole depletion of CD206<sup>+</sup> TAMs with OximUNO alleviated tumoural immunosuppression and reduced dissemination and growth, confirming the pro-tumoural and immunosuppressive roles assigned to CD206<sup>+</sup> TAMs in the literature and reaffirming the importance of targeting this particular TAM subset.

The bodyweights of mice during the treatment studies were least affected when using the OximUNO nano-formulation of DOX, in comparison with free DOX or the untargeted nano-formulation St-PGA-DOX.

Additionally, OximUNO did not alter creatinine or alanine aminotransferase levels indicating that no acute liver or kidney toxicity occurred. These are relevant findings as DOX induces cell death and tissue damage not only in the heart but also in liver and kidneys<sup>87</sup>.

Beyond TAM depletion, we here show that St-PGA-mUNO is an attractive platform that could be used in the future to carry other therapeutic payloads instead of DOX. Such payloads could include M2 $\diamond$ M1 reprogramming agents such as TRL7 agonists<sup>44,88</sup> or dodecanetetraacetic acid-chelated <sup>177</sup>Lu, for beta-emitting radiotherapy<sup>89</sup>.

Moving forward, we envisage the combination of TAM-depletion via OximUNO administration with ICIs (such as agents that block PD-1/PD-L1 pathway<sup>9,90</sup>) or current chemotherapy regimens to prevent dissemination and relapse.

## Materials And Methods

### Reagents and solutions

The peptides mUNO (sequence: CSPGAK-COOH) and FAM-mUNO (FAM-Ahx-CSPGAK-COOH) were purchased from TAG Copenhagen and doxorubicin from Sigma-Aldrich. St-PGA was kindly provided by Polypeptide Therapeutic Solution S.L. For the rest, see Supplementary Information.

Mayer's haematoxylin solution was prepared by dissolving 5 g of aluminium potassium sulphate dodecahydrate (Merck Millipore, cat. 1010421000) in 100 mL of water, then 1 g of haematoxylin (Merck, cat. H9627) was added. When it was completely dissolved, 0.02 g of sodium iodide (Merck, cat. 1065230100) was added and waited until completely dissolved. Then 2 mL of acetic acid (Sigma-Aldrich, cat. 33209) was added, and then the solution was brought to boil and cooled. Once ready to use, the solution was filtered using 0.45  $\mu$ m filter (company).

Eosin (5%) solution was prepared by dissolving 0.5 g of Eosin Y (Sigma-Aldrich, cat. 230251) in 99 mL of water and 1 mL of acetic acid.

### Cell culture and experimental animals

4T1 cells were purchased from ATCC, and 4T1-GFP cells were a gift from Ruoslahti laboratory, SBP La Jolla, USA. 4T1 and 4T1-GFP cells were cultured in a Roswell Park Memorial Institute (RPMI-1640) medium (Gibco by Life Technologies, cat. 72400-021) supplemented with 10% v/v foetal bovine serum (FBS, Capricorn Scientific, cat. FBS-11A) and 100 IU/mL penicillin/streptomycin (Capricorn Scientific, cat. PS-B) at + 37 °C in the presence of 5% CO<sub>2</sub>. For all animal experiments, 8-12-week-old female Balb/c mice were used. Animal experiment protocols were approved by the Estonian Ministry of Agriculture (Project #159). All methods were performed in accordance with existing guidelines and regulations.

### Tumour models

Two tumour models were used for homing studies: the orthotopic TNBC model, where  $1 \times 10^6$  4T1 cells in 50  $\mu\text{L}$  of phosphate-buffered saline (PBS, Lonza, cat. 17-512F) were injected subcutaneously (s.c.) into fourth mammary fat pad, and the experimental metastases of TNBC model where  $5 \times 10^5$  4T1 cells in 100  $\mu\text{L}$  of PBS were injected i.v. into Balb/c mice. Two tumour models were used for treatment studies: the orthotopic TNBC model where  $5 \times 10^4$  4T1 cells in 50  $\mu\text{L}$  of PBS were injected s.c. into fourth mammary fat pad; and the experimental metastases of TNBC model where  $2 \times 10^5$  4T1 cells in 100  $\mu\text{L}$  of PBS were injected i.v.

## Synthesis and characterisation of nanoconjugates

Four different nanoconjugates were used. For in vivo homing studies St-PGA-OG and St-PGA-OG-mUNO were used, and for in vitro cytotoxicity and in vivo treatment studies St-PGA-DOX and St-PGA-DOX-mUNO (“OximUNO”) were used. DOX here denotes doxorubicin. Detailed synthetic procedure for single nanoconjugates can be found in Supplementary Information.

## Physico-chemical characterisation methods

Nuclear magnetic resonance (NMR) spectroscopy: NMR spectra were recorded at  $27^\circ\text{C}$  (300 K) on a 300 Ultrashield<sup>TM</sup> from Bruker. Data were processed with the software Mestrenova. Sample solutions were prepared at the desired concentration in  $\text{D}_2\text{O}$  or  $\text{D}_2\text{O}$  supplemented with  $\text{NaHCO}_3$  (0.5 M).

UV-Visible (UV-Vis) analysis: The UV-Vis measurements were performed using JASCO V-630 spectrophotometer at  $25^\circ\text{C}$  with 1 cm quartz cells and a spectral bandwidth of 0.5 nm. Spectra analysis was recorded three times in the range of 200–700 nm.

Fluorescence analysis: The fluorescence analysis was performed using a JASCO FP-6500 spectrofluorimeter at  $25^\circ\text{C}$  with 1 cm quartz cells.

Dynamic Light Scattering (DLS): Size measurements were performed using a Malvern ZetasizerNano ZS instrument, supported by a 532 nm laser at a fixed scattering angle of  $173^\circ$ . Nanoconjugate solutions (0.1 mg/mL) were freshly prepared in PBS (10 mM phosphate, 150 mM NaCl), filtered through a 0.45  $\mu\text{m}$  cellulose membrane filter, and measured. Size distribution was measured (diameter, nm) for each polymer in triplicate. Automatic optimisation of beam focusing and attenuation was applied for each sample.

Zeta potential measurements: The Zeta potential measurements were performed at  $25^\circ\text{C}$  using a Malvern ZetasizerNano ZS instrument, equipped with a 532 nm laser using Disposable folded capillary cells, provided by Malvern Instruments Ltd. Nanoconjugate solutions (0.1 mg/mL) were freshly prepared in 1 mM KCl. The solutions were filtered through a 0.45  $\mu\text{m}$  cellulose membrane filter. Zeta potential was measured for each sample per triplicate.

## Molecular dynamics simulations

Molecular dynamics (MD) simulations of the nanoconjugate, polyglutamate chains and mUNO peptide were carried out using the ff19SB force field<sup>91</sup> in the Amber20 MD engine<sup>92</sup>. The nanoconjugate system was neutralised using Na<sup>+</sup> ions and hydrated to account for a total of ~ 920 000 atoms (~ 300 000 TIP3P water molecules) in a truncated octahedral box. A hydrogen mass repartitioning strategy was applied on the resulting topology, allowing us to use a 4 fs integration time step<sup>93</sup>. We used standard minimisation and equilibration protocols to reach 300 K and 1 atm., followed by 50 ns of production MD run. The simulations were run under the NVT ensemble (constant number of particles, volume, and temperature through Berendsen thermostat<sup>94</sup>), considering periodic boundary conditions. To fix hydrogen atoms, the SHAKE algorithm was used<sup>95</sup>. The non-bound cut-off value was set to Angstrom. We parametrised the central moiety of the nanoconjugate using the recommended protocol for the Amber force field. It was necessary to introduce amide bond, angle and dihedral terms using ParmEd module to establish the bond of the central molecule to the polyglutamate chains.

## Tumour homing studies

Tumours were induced as described in tumour models' section. Tumour homing studies were performed on mice bearing orthotopic TNBC or experimental metastases of TNBC. Ten days p.i. of the orthotopic TNBC or the experimental metastases of TNBC, mice were injected i.p. with St-PGA-OG-mUNO (0.41 mg/0.5mL of PBS) or St-PGA-OG (0.35 mg/0.5mL of PBS) (corresponding to 15nmoles of OG, fluorescence measured by UV-Vis). We also analysed the homing of a higher dose of St-PGA-PGA-mUNO (0.82 mg/0.5mL of PBS) or St-PGA-OG (0.7 mg/0.5mL of PBS) (corresponding to 30nmoles of OG) and compared it with the homing of FAM-mUNO (30nmoles/0.5mL of PBS). In every case, the nanoconjugates or free peptide were circulated for 6h, after which mice were sacrificed by anaesthetic overdose followed by cervical dislocation. Organs and tumours were collected and fixed in cold 4% w/v paraformaldehyde (PFA) in PBS at + 4°C for 24h, washed in PBS at RT for 1 h and cryoprotected in 15% w/v sucrose (Sigma Life Science, cat. S9378) followed by 30% w/v sucrose at + 4 °C overnight. Cryoprotected and fixed tissues were frozen in OCT (Optimal Cutting Temperature, Leica, cat. 14020108926), cryosectioned at 10 µm on Superfrost+ slides (Thermo Fisher, cat. J1800AMNZ) and stored at -20°C. Immunofluorescent staining was performed as described earlier<sup>42</sup>. OG was detected using rabbit anti-FITC/Oregon Green (dilution 1/100, Invitrogen by Thermo Fisher Scientific, cat. A889) and Alexa Fluor® 647 goat anti-rabbit antibody (dilution 1/250, Invitrogen by Thermo Fisher Scientific, cat. A21245). CD206 was detected using rat anti-mouse CD206 (dilution 1/150, Bio-Rad, cat. MCA2235GA) and Alexa Fluor® 546 goat anti-rat antibody (dilution 1/250, life technologies, cat. A11081). CD86 was detected using rat anti-mouse CD86 (dilution 100, BioLegend, cat. 105001) and Alexa Fluor® 546 goat anti-rat secondary antibody (dilution 1/250). CD11c was detected using hamster anti-mouse CD11c antibody (dilution 1/75, BioLegend, cat. 117301) and Alexa Fluor® 546 goat anti-hamster secondary antibody (dilution 1/200, life technologies, cat. A21111) Slides were counterstained using 4',6-diamidino-2-phenylindole (DAPI, 1 µg/mL, Sigma-Aldrich, cat. D9542-5MG). The coverslips were mounted using mounting medium (Fluoromount-G™ Electron Microscopy Sciences, cat. 17984-25), and sections were imaged using Zeiss confocal microscope (Zeiss LSM-710) and 20x objective. Colocalisation analysis was carried out using the Fiji programme and Pearson's coefficient, and average

values were obtained using three images per mouse per group. OG/FAM mean signal per CD206<sup>+</sup> cell analysis was carried out using the ImageJ programme, taking mean OG/FAM signal, and dividing it with the number of CD206<sup>+</sup> cells. Average values were obtained from four images per mouse. N = 3 for orthotopic TNBC and N = 2 for the homing in experimental metastases of TNBC.

## Plasma half-life evaluation for St-PGA-OG-mUNO

Plasma half-life studies were performed as previously described<sup>42</sup>. Shortly, healthy female Balb/c mice (N = 3) were injected i.p. with St-PGA-OG-mUNO (0.41 mg/0.5mL of PBS, corresponding to 15nmoles of OG). Ten  $\mu$ L of blood was taken at different timepoints (0, 5, 10, 15, 30, 60, 180, 360, 1440 min) and mixed with 50  $\mu$ L of PBS-Heparin solution. Blood samples were centrifuged to obtain plasma (300g for 5 min at RT) and OG fluorescence was read with a plate reader (FlexStation II Molecular Devices) at 480nm excitation, 520nm emission.

## DOX release studies

The LC-MS was implemented in the determination of free drug, stability, and drug release studies of OximUNO conjugate. The LC-MS consisted of ExionLC LC system and AB Sciex QTRAP 4500, a triple quadrupole ion trap hybrid equipped with Turbo VTM electrospray ionisation source. DOX was determined with an internal standard method: 1  $\mu$ g/mL of daunorubicin (DAU) was used as internal standard where three calibration curves (in a range from 0.5 to 50  $\mu$ g/mL DOX) were prepared and used for accurate analysis of DOX in the samples. Both DOX and DAU were detected with positive electrospray ionisation mode by following two mass transitions (544.2 m/z  $\rightarrow$  397 m/z and 544.2 m/z  $\rightarrow$  379 m/z for DOX, and 528 m/z  $\rightarrow$  363.1 m/z and 528 m/z  $\rightarrow$  321.3 m/z for DAU). The obtained LC-MS optimal conditions were as follows: flow rate 0.5 mL/min; mobile phase – 0.05 % trifluoroacetic acid with 70 % of acetonitrile; LiChrospher 100 C18 column (125x4.0 mm) (Merck); column temperature 40 °C, 10  $\mu$ L injection volume.

### Stability study of OximUNO conjugate in PBS, pH 7.4

OximUNO conjugate was incubated in 10 mM dPBS at 37°C at the concentration of 3 mg/mL and with 3  $\mu$ g/mL of DAU. 100  $\mu$ L of aliquot was collected at defined time points (0, 1, 2, 5, 24, 48, 72 h) extracted with 3x250  $\mu$ L chloroform and mixed with vortex for 5 min. Organic phases from all three chloroform extracts were collected in one tube, evaporated using speed vacuum until dry, and stored at -20°C. On the day of analysis, dried samples were reconstituted in 300  $\mu$ L of methanol (LC-MS grade), vortexed for 5 min and centrifuged for 5 min at 30 437g. Supernatants were filtered through 0.45  $\mu$ m filter and subjected to the LC-MS analysis.

### Stability study of OximUNO in the i.p. fluid

The i.p fluid was collected from healthy 8-12-week old Balb/c female mice as performed by Ray and Dittel<sup>96</sup> by collecting the supernatant and discarding the pellet after the centrifugation step. A working solution containing 3 mg/mL of OximUNO and 3  $\mu$ g/mL of DAU in i.p. fluid was incubated at 37°C. 50  $\mu$ L

aliquots were collected at scheduled time points (0, 2, 5, 7, 24 h). The samples were then diluted with 100  $\mu$ L of methanol and sonicated to aid the dissolution of DOX. The samples were injected into LC-MS after filtration through 0.45  $\mu$ m filter.

Cathepsin B release kinetic studies.

Cathepsin B (5 IU) was activated in 2 mM EDTA, 5 mM DTT, and 20 mM  $\text{CH}_3\text{COONa}$  buffer and incubated at 37°C for 15 min. In a separate tube, a solution containing 3 mg/mL OximUNO and 3  $\mu$ g/mL of DAU was prepared with 20 mM  $\text{CH}_3\text{COONa}$  and incubated at 37°C for 15 min. The two solutions were then combined producing reaction solution that was incubated at 37°C. 100  $\mu$ L aliquots were collected at scheduled time points (0, 1, 2, 5, 8, 24, 48, 72 h), and after the addition of 900  $\mu$ L of dPBS (to adjust the pH level to 7.4), the free DOX and DAU were extracted with three portions of 2.5 mL of  $\text{CHCl}_3$ . Samples were proceeded as described under “Stability study of OximUNO conjugate in PBS, pH 7.4”. After  $\text{CHCl}_3$  evaporation, the samples were reconstituted with 300  $\mu$ L of methanol, filtered through a 0.45  $\mu$ m filter and subjected to LC-MS analysis. A blank solution was prepared with the same components as sample solution but without cathepsin B and used as a control sample.

## In vitro cytotoxicity assay

Human peripheral blood mononuclear cells (PBMC) were purified from human blood buffy coat using Ficoll Paque Plus (GE Healthcare, cat. 17-1440-02) reagent and CD14<sup>+</sup> microbeads (MACS Miltenyi Biotec, cat. 130-050-201) as described before<sup>42</sup>.  $1.2 \times 10^5$  cells in 50  $\mu$ L of RPMI-1640 medium were seeded on FBS-coated 96-well plate. To obtain optimal macrophage attachment and polarisation towards M2 phenotype, 50  $\mu$ L of IL-4 (50 ng/mL, BioLegend, cat. 574002) and M-CSF (100 ng/mL, BioLegend, cat. 574802) mixture in the medium was added to the wells. The medium was replenished by substituting the half of the medium with fresh medium containing IL-4 and M-CSF every other day for six days. To obtain M1 macrophages, the monocytes were incubated with M-CSF (100 ng/mL) for six days, replenishing every other day with fresh medium containing M-CSF and on day six, 50  $\mu$ L of M-CSF, LPS (100 ng/mL, Sigma Aldrich, cat. L4391) and IFN- $\gamma$  (20 ng/mL, BioLegend, cat. 570202) mixture was added and incubated overnight in the incubator. On day seven, M2 and M1 macrophages were incubated for 15 min at 37 °C with OximUNO, St-PGA-DOX, DOX, or free medium as a control (N = 3 wells per group). Concentrations used were calculated based on DOX: 33 $\mu$ M and 100 $\mu$ M. After incubation, wells were washed, new medium added and incubated for 48 h at 37 °C. After 48 h, 10  $\mu$ L of 3-(4,5-Dimethylthiazol-2-yl)-2,5-Diphenyltetrazolium Bromide (MTT, concentration 5 mg/mL, Invitrogen, cat. M6494) in PBS was added to each well containing culture medium and incubated for 2.5 h at 37 °C after which medium containing MTT was removed without removing formed crystals and 100  $\mu$ L of isopropanol was added to each well to dissolve crystals. Then, absorbance was read at 580nm using plate reader (Tecan Sunrise) and corresponding Magellan™ 7 programme.

## In vivo liver and kidney toxicology studies with OximUNO

Three healthy 12-week-old female Balb/c mice were injected i.p. with OximUNO (704 µg/0.5mL PBS) and circulated for 48 h. Then, mice were anesthetised, and blood was collected through retro-orbital bleeding into Lithium Heparin tubes (BD Vacutainer, cat. 368494). Blood samples were centrifuged at 1800g for 15 min at + 4 °C and 400 µL of plasma was collected for analysis. Samples were analysed in Tartu University Hospital using a Cobas 6000 IT-MW (Roche Diagnostics GmbH) machine and reagents for creatinine (CREP2, cat. 03263991) and alanine aminotransferase (ALTLP, cat. 04467388).

## **Monotherapy with OximUNO in the orthotopic TNBC**

$5 \times 10^4$  4T1 cells in 50 µL of PBS were injected s.c. into the fourth mammary fat pad of 8-12-week-old female Balb/c mice. On day seven, mice were sorted into four groups by their tumour volume measured using digital calliper (Mitutoyo). Tumour volume was calculated based on the formula  $(W^2 \times L)/2$ , where W is the tumour's width and L is the tumour's length. The starting volume for each group was  $\sim 25 \text{ mm}^3$ , and the number of mice in each group was five. The first i.p. injection of compounds was carried out on day seven, followed by i.p injection every other day; nine injections were performed in total. The dose of the nanoconjugates was calculated based on DOX, 2mg/kg per injection (DOX: 39.5 µg/0.5mL PBS; St-PGA-DOX: 476 µg/0.5mL PBS; OximUNO: 341 µg/0.5mL PBS) giving a cumulative dose of DOX of 18mg/kg. Mice bodyweight and tumour volumes were monitored every other day. The final injection was on day 25 and all mice were sacrificed on day 28. Tumour tissues were processed as described under "In vivo biodistribution studies", and the lungs and hearts were embedded in paraffin and processed for haematoxylin and eosin (H&E) staining (described below). Tumours were immunostained as described above. CD206 was detected using rat anti-mouse CD206 (dilution 1/200), CD8 using rat anti-mouse CD8 (dilution 1/75 Biologend, cat. number 100701), and FOXP3 using rat anti-mouse FOXP3 (dilution 1/75, Biologend, cat number 126401) as primary antibodies. Alexa Fluor® goat anti-rat 647 (dilution 1/300 for CD206 and 1/200 for CD8 and FOXP3) was used as secondary antibody for all markers. Slides were counterstained with DAPI (1 µg/mL in PBS). All 5 tumours from each group were included into the IF analysis. Fluorescent signal intensity was calculated using ImageJ programme, wherein the mean values from at least three images per tumour were included.

## **H&E staining on paraffin-embedded formalin-fixed tissues**

For H&E staining, 2 µm sections were cut from paraffin-embedded blocks. Then slides were warmed at 60 °C for 2 min before deparaffinising using xylene (3x2 min, 1x1 min) followed by 100% ethanol washes (3x1 min), 80% ethanol wash (1x1 min) followed by 1 min wash in water. Slides were first incubated with ST-1 HemaLast for 30 s, followed by ST-2 Haematoxylin for 5 min after which slides were washed in water for 2 min. Then, ST-3 Differentiator was added for 45 s, and slides were washed in water for 1 min. Next, ST-4 Bluing Agent was added (1 min), washed for 1 min in water followed by 1 min incubation in 80% ethanol, after which ST-5 Eosin was added and incubated for 1 min. For rehydration, incubations in 100% ethanol (2x30 s, 1x2 min) were carried out and finished with incubations in xylene (2x2 min). All washes were carried out in tap water. H&E stainings were performed in Tartu University Hospital by pathologists using Leica staining automat and ST Infinity H&E Staining System (Leica, cat. 38016998). Stained lung sections were scanned using slide scanner (Leica SCN400) and 20x zoom. Pictures were

analysed using QuPath programme (version 0.1.2)<sup>97</sup>. Five levels ~ 1 mm apart were used for each mouse to obtain comprehensive metastases profile of the lungs. Stained heart sections were also scanned using slide scanner and analysed with QuPath programme. Tartu University Hospital pathologists assessed cardiotoxicity in hearts and pulmonary metastases.

## **Monotherapy with OximUNO in the experimental metastases of TNBC**

$2 \times 10^5$  4T1 cells in 100  $\mu$ L of PBS were injected i.v. in the tail vein of 8-12-week-old female Balb/c mice. Treatment with OximUNO, St-PGA-DOX, or DOX was started on day four p.i.; each group had six mice. Doses of different compounds were calculated based on DOX (2mg/kg): DOX: 39.5  $\mu$ g/0.5mL PBS; St-PGA-DOX: 774.5  $\mu$ g/0.5mL PBS; OximUNO: 704  $\mu$ g/0.5mL PBS. The bodyweight of each mouse was monitored every other day. A total of six injections were carried out every other day. The final injection was on day 12, and all animals were sacrificed on day 18 using anaesthetic overdose and perfusion with PBS. Three right lungs from each group went to the flow cytometry (FC) analysis, and three full lungs and three left ones from each group were frozen into block using OCT. Frozen lung tissues were cryosectioned as described earlier, fixed with cold 4% PFA (CD206) or acetone (for CD8 and FOXP3), and stained as described in following section. Immunofluorescent stainings were performed using the same markers and antibodies as shown in “Monotherapy with OximUNO on orthotopic TNBC model” section.

### **GFP staining and imaging**

Six lungs from each group were frozen in OCT. 10  $\mu$ m sections were cut, and slides were kept at -20 °C until ready to use. Slides were taken out of the freezer at least 30 min before staining. For staining, slides were fixed with 4% PFA for 10 min at RT, washed with PBS for 10 min at RT, counterstained using DAPI (1  $\mu$ g/mL) for 5 min at RT, washed 3x4 min with PBS and finally mounted using mounting medium. Permeabilisation was not used in this step to improve GFP visualisation. GFP was visualised using its native fluorescence. Slides were imaged using Olympus confocal microscope (FV1200MPE) using a 10x objective.

### **Macroscopic analysis of GFP signal**

Lungs from each group were imaged using Illumatool Bright Light System LT-9900 (LightTool's Research) in green channel to visualise the fluorescent signal macroscopically, and a photograph of each lung was taken. The total GFP signal of each lung was quantified using ImageJ programme using “IntDen” value.

### **Flow cytometry (FC) analysis**

Three mice were sacrificed using anaesthetic overdose, perfused with PBS and right lung tissues were placed in cold RPMI-1640 medium supplemented with 2% v/v FBS. Lungs were cut into small pieces on ice in a solution containing collagenase IV (160 U/mL, Gibco cat.17104019)/dispase (0.6 U/mL, Gibco, cat. 17105-041)/DNase I (15 U/mL; AppliChem, cat. A3778) mixture. To obtain single cell suspension, lung pieces were incubated in 10 mL of the same mixture at 37 °C on a rotating platform for 45–60 min, pipetting every 10 min to improve digestion. The cells were washed with 5 mL of RB (“running buffer”: 4

mL 0.5M EDTA, 100 mL v/v FBS in 1L of PBS), centrifuged (all centrifugations at 350g for 7 min at + 4 °C), and red blood cells were lysed with 3 mL of Ammonium-Chloride-Potassium Lysing Buffer (ACK) at RT. Ten mL of RB was added, cells were centrifuged and filtered using 100 µm cell strainer (Falcon, cat. 352360). Cells were counted using the brightfield mode of LUNA™ Automated Cell counter (Logos Biosystems). The cells were taken up in RB at a concentration of  $5 \times 10^6 / 100 \mu\text{L}$ , placed on a 96-well plate with conical bottom and incubated for 30 min in FcR-blocking 2.4G2 hybridoma medium at + 4 °C. The cells were then stained for either macrophage or T cell markers for 25–45 min in the dark at + 4 °C, centrifuged and washed twice with RB. Antibodies used are listed in Table 2. For intracellular staining of T cells, cells were fixed using eBioscience™ FOXP3/Transcription Factor Staining Buffer Set (Thermo Fisher, cat. 00-5523-00) according to the protocol provided. Following permeabilisation, cells were stained for 25–45 min in the dark at RT and washed twice using RB. All the cells were taken up in 150 µL of RB, filtered through a 70 µm filter (Share Group Limited) and 150 µL of RB was used to wash the filter. BD LSRFortessa Flow Cytometer and FCS Express 7 Flow (De Novo Software) were used for analysis.

Table 2  
Antibodies used in FC analysis: macrophage and T cell markers.

Macrophage markers	Antibody	Dilution, company
	PerCP/Cyanine5.5 anti-mouse CD206 (MMR)	1/200, BioLegend, clone C068C2, cat. 141715
	PE anti-mouse CD86	1/400, BioLegend, clone PO3, cat. 105105
	PE/Cyanine7 anti-mouse F4/80	1/200, BioLegend, clone BM8, cat. 123114
	PE/Dazzle™ 594 anti-mouse/human CD11b	1/ 800, BioLegend, clone M1/70, cat. 101255
	eBioscience™ Fixable Viability Due eFluor™ 506	1/800, Thermo Fisher Scientific, cat. 65-0866-18
T cell markers	Brilliant Violet 570™ anti-mouse CD4	1/400, BioLegend, clone RM4-5, cat. 100542
	Brilliant Violet 605™ anti-mouse CD8a	1/400, BioLegend, clone 53 – 6.7, cat. 100744
	PE/Dazzle™ 594 anti-mouse CD279 (PD-1)	1/200, BioLegend, clone 29F.1A12, cat. 135228
	Alexa Fluor® 488 anti-mouse FOXP3	1/100, BioLegend, clone MF-14, cat 126406
	PerCP/Cyanine5.5 anti-mouse CD3ε	1/200, BioLegend, clone 145-2C11, cat. 100328
	Brilliant Violet 421™ anti-mouse CD152 (CTLA4)	1/200, BioLegend, clone UC10-4B9, cat. 106312
	eBioscience™ Fixable Viability Due eFluor™ 506	1/800, Thermo Fisher Scientific, cat. 65-0866-18

## H&E staining on PFA fixed cryosections

Ten µm sections were cut from unfixed tissues in a frozen block; sections were stored at -20 °C until ready to use. When ready, slides were taken out of the freezer at least 30 min before staining. Room temperature slides were fixed with cold 4% PFA for 10 min at RT followed by washing in PBS for 10 min at RT. After washing, slides were dipped into Mayer's haematoxylin solution (see preparation under "Reagents and solution") for 10 s, followed by washing in running tap water for 5 min. Then, slides were dipped into Eosin (5%) solution (see preparation under "Reagents and solution") for 20 s, followed by washing in running tap water for 5 min. For rehydration, slides were placed first in 96% ethanol (2x2min) followed by 100% ethanol (2x2min). For clearance slides were placed in RotiClear® solution (Roth, cat. A538.5) for 2x5 min after which slides were mounted using Eukitt® quick-hardening mounting medium

(Merck, cat. 03989). Slides were scanned using Leica DM6 B microscope and Leica Aperio Versa 8 slides scanner with 20x zoom and pictures were analysed using ImageScope programme (version 12.3.3).

## **Statistical analysis**

All statistical analysis was carried out using One-Way ANOVA, Fisher LSD test, using a Statistica programme (release 7).

## **Data Availability**

All data needed to evaluate the conclusions on the paper are presented in the paper and/or the Supplementary Information. Additional data related to the findings of this study are available from the corresponding authors.

## **Declarations**

### **ACKNOWLEDGEMENTS**

We would like to thank dr. Stuart P. Atkinson for English editing and proofreading the manuscript, Merje Jakobson for performing H&E studies on paraffin-embedded formalin fixed tissues, dr. Aivar Orav for in vivo toxicity study analysis and dr. Mario Plaas for the help with slide scanner. P.S. acknowledges support by the Estonian Research Council (grant: PUT PSG38 to P.S.) and a Feasibility fund of University of Tartu (grant: ARENG51 to P.S.). A.L. acknowledges a PhD fellowship from the Estonian government. M.J.V. acknowledges the support by European Research Council grants (ERC-CoG-2014-648831 “My-Nano” and ERC-PoC-2018-825798 “Polymune”). Part of the equipment employed in this work has been funded by Generalitat Valenciana and co-financed with FEDER funds (PO FEDER of Comunitat Valenciana 2014–2020). U.H acknowledges the support by EsRC Mobilitas+ grant MOBTP185. T.T. acknowledges the support by UT EIK grant and GMVBS0230PR.

### **AUTHOR CONTRIBUTIONS**

A.L. performed the in vitro and in vivo experiments, histology, immunofluorescence, flow cytometry, analysis and wrote the manuscript. A.M. performed chemical design, synthesis, and characterisation and edited the manuscript. U.H. performed flow cytometry experiments and analysis. E.A., M.P. and M.B. performed computational simulations. S.D. performed drug release studies and chemical characterisation. L.S. performed analysis and expert evaluation of H&E images. P.P. edited the manuscript and provided discussions and lab support. T.T. edited the manuscript, participated in the experimental design and discussions, and provided the lab support. M.J.V. performed chemical design, design of in vitro and in vivo experiments, supervision of chemical synthesis and characterisation, provided lab support and edited the manuscript. P.S. supervised all the experiments, participated in their design and analysis, and edited the manuscript. All authors edited the manuscript and approved the final version.

### **CORRESPONDING AUTHORS**

## ETHICS DECLARATIONS

## COMPETING INTERESTS

P.S. and T.T. are inventors of patents on mUNO peptide. M.J.V. is an inventor of a patent on BTA-core branched polypeptides (including St-PGA) licensed to PTS SL. In addition, T.T. is an inventor of iRGD and CendR peptides and a shareholder of Cend Therapeutics Inc., a company that holds a license for the mUNO, iRGD and CendR peptides.

## References

1. Rivenbark, A. G., O'Connor, S. M. & Coleman, W. B. Molecular and cellular heterogeneity in breast cancer: challenges for personalized medicine. *Am. J. Pathol.* **183**, 1113–1124 (2013).
2. Foulkes, W. D., Smith, I. E. & Reis-Filho, J. S. Triple-Negative Breast Cancer. *N. Engl. J. Med.* **363**, 1938–1948 (2010).
3. Lehmann, B. D. *et al.* Identification of human triple-negative breast cancer subtypes and preclinical models for selection of targeted therapies. *J. Clin. Invest.* **121**, 2750–2767 (2011).
4. Garrido-Castro, A. C., Lin, N. U. & Polyak, K. Insights into Molecular Classifications of Triple-Negative Breast Cancer: Improving Patient Selection for Treatment. *Cancer Discov.* **9**, 176–198 (2019).
5. Pardoll, D. M. The blockade of immune checkpoints in cancer immunotherapy. *Nat. Rev. Cancer* **12**, 252–264 (2012).
6. Esfahani, K. *et al.* A Review of Cancer Immunotherapy: From the Past, to the Present, to the Future. *Curr. Oncol.* **27**, 87–97 (2020).
7. Adams, S. *et al.* Current Landscape of Immunotherapy in Breast Cancer: A Review. *JAMA Oncol.* **5**, 1205–1214 (2019).
8. Gong, J., Chehrazi-Raffle, A., Reddi, S. & Salgia, R. Development of PD-1 and PD-L1 inhibitors as a form of cancer immunotherapy: a comprehensive review of registration trials and future considerations. *J. Immunother. Cancer* **6**, 8 (2018).
9. Schmid, P. *et al.* Atezolizumab and Nab-Paclitaxel in Advanced Triple-Negative Breast Cancer. *N. Engl. J. Med.* **379**, 2108–2121 (2018).
10. Schmid, P. *et al.* Atezolizumab plus nab-paclitaxel as first-line treatment for unresectable, locally advanced or metastatic triple-negative breast cancer (IMpassion130): updated efficacy results from a randomised, double-blind, placebo-controlled, phase 3 trial. *Lancet Oncol.* **21**, 44–59 (2020).
11. Marra, A., Viale, G. & Curigliano, G. Recent advances in triple negative breast cancer: the immunotherapy era. *BMC Med.* **17**, 90 (2019).
12. Mori, H. *et al.* The combination of PD-L1 expression and decreased tumor-infiltrating lymphocytes is associated with a poor prognosis in triple-negative breast cancer. *Oncotarget* **8**, 15584–15592

- (2017).
13. Mittendorf, E. A. *et al.* PD-L1 Expression in Triple-Negative Breast Cancer. *Cancer Immunol. Res.* **2**, 361–370 (2014).
  14. Socinski, M. A. *et al.* Atezolizumab for First-Line Treatment of Metastatic Nonsquamous NSCLC. *N. Engl. J. Med.* **378**, 2288–2301 (2018).
  15. Adams, S. *et al.* Patient-reported outcomes from the phase III IMpassion130 trial of atezolizumab plus nab-paclitaxel in metastatic triple-negative breast cancer. *Ann. Oncol.* **31**, 582–589 (2020).
  16. Fecher, L. A., Agarwala, S. S., Hodi, F. S. & Weber, J. S. Ipilimumab and Its Toxicities: A Multidisciplinary Approach. *The Oncologist* **18**, 733–743 (2013).
  17. Hunter, G., Voll, C. & Robinson, C. A. Autoimmune inflammatory myopathy after treatment with ipilimumab. *Can. J. Neurol. Sci. J. Can. Sci. Neurol.* **36**, 518–520 (2009).
  18. Maker, A. V. *et al.* Tumor Regression and Autoimmunity in Patients Treated With Cytotoxic T Lymphocyte–Associated Antigen 4 Blockade and Interleukin 2: A Phase I/II Study. *Ann. Surg. Oncol.* **12**, 1005–1016 (2005).
  19. Phan, G. Q. *et al.* Cancer regression and autoimmunity induced by cytotoxic T lymphocyte-associated antigen 4 blockade in patients with metastatic melanoma. *Proc. Natl. Acad. Sci. U. S. A.* **100**, 8372–8377 (2003).
  20. Cretella, D. *et al.* Pre-treatment with the CDK4/6 inhibitor palbociclib improves the efficacy of paclitaxel in TNBC cells. *Sci. Rep.* **9**, 13014 (2019).
  21. Arola, O. J. *et al.* Acute Doxorubicin Cardiotoxicity Involves Cardiomyocyte Apoptosis. *Cancer Res.* **60**, 1789–1792 (2000).
  22. Zhang, S. *et al.* Identification of the molecular basis of doxorubicin-induced cardiotoxicity. *Nat. Med.* **18**, 1639–1642 (2012).
  23. Keklikoglou, I. *et al.* Chemotherapy elicits pro-metastatic extracellular vesicles in breast cancer models. *Nat. Cell Biol.* **21**, 190–202 (2019).
  24. Hughes, R. *et al.* Perivascular M2 Macrophages Stimulate Tumor Relapse after Chemotherapy. *Cancer Res.* **75**, 3479–3491 (2015).
  25. Lewis, C. E. & Pollard, J. W. Distinct Role of Macrophages in Different Tumor Microenvironments. *Cancer Res.* **66**, 605–612 (2006).
  26. Peranzoni, E. *et al.* Macrophages impede CD8 T cells from reaching tumor cells and limit the efficacy of anti-PD-1 treatment. *Proc. Natl. Acad. Sci.* **115**, E4041–E4050 (2018).
  27. Neubert, N. J. *et al.* T cell–induced CSF1 promotes melanoma resistance to PD1 blockade. *Sci. Transl. Med.* **10**, eaan3311 (2018).
  28. Daurkin, I. *et al.* Tumor-Associated Macrophages Mediate Immunosuppression in the Renal Cancer Microenvironment by Activating the 15-Lipoxygenase-2 Pathway. *Cancer Res.* **71**, 6400–6409 (2011).
  29. Gok Yavuz, B. *et al.* Cancer associated fibroblasts sculpt tumour microenvironment by recruiting monocytes and inducing immunosuppressive PD-1 + TAMs. *Sci. Rep.* **9**, 3172 (2019).

30. Pathria, P., Louis, T. L. & Varner, J. A. Targeting Tumor-Associated Macrophages in Cancer. *Trends Immunol.* **40**, 310–327 (2019).
31. DeNardo, D. G. *et al.* Leukocyte Complexity Predicts Breast Cancer Survival and Functionally Regulates Response to Chemotherapy. *Cancer Discov.* **1**, 54–67 (2011).
32. Mancini, V. S. B. W., Pasquini, J. M., Correale, J. D. & Pasquini, L. A. Microglial modulation through colony-stimulating factor-1 receptor inhibition attenuates demyelination. *Glia* **67**, 291–308 (2019).
33. Lee, S., Shi, X. Q., Fan, A., West, B. & Zhang, J. Targeting macrophage and microglia activation with colony stimulating factor 1 receptor inhibitor is an effective strategy to treat injury-triggered neuropathic pain. *Mol. Pain* **14**, 1744806918764979 (2018).
34. Bissinger, S. *et al.* Macrophage depletion induces edema through release of matrix-degrading proteases and proteoglycan deposition. *Sci. Transl. Med.* **13**, eabd4550 (2021).
35. Wesolowski, R. *et al.* Phase Ib study of the combination of pexidartinib (PLX3397), a CSF-1R inhibitor, and paclitaxel in patients with advanced solid tumors. *Ther. Adv. Med. Oncol.* **11**, 1758835919854238 (2019).
36. Papadopoulos, K. P. *et al.* First-in-Human Study of AMG 820, a Monoclonal Anti-Colony-Stimulating Factor 1 Receptor Antibody, in Patients with Advanced Solid Tumors. *Clin. Cancer Res.* **23**, 5703–5710 (2017).
37. Kitamura, T. *et al.* Monocytes Differentiate to Immune Suppressive Precursors of Metastasis-Associated Macrophages in Mouse Models of Metastatic Breast Cancer. *Front. Immunol.* **8**, (2018).
38. Madsen, D. H. *et al.* Tumor-Associated Macrophages Derived from Circulating Inflammatory Monocytes Degrade Collagen through Cellular Uptake. *Cell Rep.* **21**, 3662–3671 (2017).
39. Ishihara, D. *et al.* Wiskott-Aldrich Syndrome Protein Regulates Leukocyte-Dependent Breast Cancer Metastasis. *Cell Rep.* **4**, 429–436 (2013).
40. Karousou, E. *et al.* Collagen VI and Hyaluronan: The Common Role in Breast Cancer. *BioMed Res. Int.* **2014**, 1–10 (2014).
41. Scodeller, P. *et al.* Precision Targeting of Tumor Macrophages with a CD206 Binding Peptide. *Sci. Rep.* **7**, 14655 (2017).
42. Lepland, A. *et al.* Targeting Pro-Tumoral Macrophages in Early Primary and Metastatic Breast Tumors with the CD206-Binding mUNO Peptide. *Mol. Pharm.* **17**, 2518–2531 (2020).
43. Ascitutto, E. K. *et al.* Phage-Display-Derived Peptide Binds to Human CD206 and Modeling Reveals a New Binding Site on the Receptor. *J. Phys. Chem. B* **123**, 1973–1982 (2019).
44. Figueiredo, P. *et al.* Peptide-guided resiquimod-loaded lignin nanoparticles convert tumor-associated macrophages from M2 to M1 phenotype for enhanced chemotherapy. *Acta Biomater.* (2020).
45. Arroyo-Crespo, J. J. *et al.* Tumor microenvironment-targeted poly-L-glutamic acid-based combination conjugate for enhanced triple negative breast cancer treatment. *Biomaterials* **186**, 8–21 (2018).
46. Duro-Castano, A. *et al.* Polyglutamic acid-based crosslinked doxorubicin nanogels as an anti-metastatic treatment for triple negative breast cancer. *J. Controlled Release* **332**, 10–20 (2021).

47. Arroyo-Crespo, J. J. *et al.* Anticancer Activity Driven by Drug Linker Modification in a Polyglutamic Acid-Based Combination-Drug Conjugate. *Adv. Funct. Mater.* **28**, 1800931 (2018).
48. Shaffer, S. A. *et al.* In vitro and in vivo metabolism of paclitaxel poliglumex: identification of metabolites and active proteases. *Cancer Chemother. Pharmacol.* **59**, 537–548 (2007).
49. Gordon, S. R. *et al.* PD-1 expression by tumour-associated macrophages inhibits phagocytosis and tumour immunity. *Nature* **545**, 495–499 (2017).
50. Zhang, M. *et al.* Anti-CD47 Treatment Stimulates Phagocytosis of Glioblastoma by M1 and M2 Polarized Macrophages and Promotes M1 Polarized Macrophages In Vivo. *PLOS ONE* **11**, e0153550 (2016).
51. Simon-Gracia, L. *et al.* Bifunctional Therapeutic Peptides for Targeting Malignant B Cells and Hepatocytes: Proof of Concept in Chronic Lymphocytic Leukemia. *Adv. Ther.* **3**, 2000131 (2020).
52. MPD: Phenotype strain survey measures: alanine aminotransferase. <https://phenome.jax.org/search/details/ssmeasures?searchterm=alanine+aminotransferase+&ontavail=2>.
53. BALB/c Mouse | Charles River Laboratories. <https://www.criver.com/products-services/find-model/balbc-mouse?region=3616>.
54. Cassetta, L. & Kitamura, T. Targeting Tumor-Associated Macrophages as a Potential Strategy to Enhance the Response to Immune Checkpoint Inhibitors. *Front. Cell Dev. Biol.* **0**, (2018).
55. Santoni, M. *et al.* Triple negative breast cancer: Key role of Tumor-Associated Macrophages in regulating the activity of anti-PD-1/PD-L1 agents. *Biochim. Biophys. Acta BBA - Rev. Cancer* **1869**, 78–84 (2018).
56. Rodell, C. B. *et al.* TLR7/8-agonist-loaded nanoparticles promote the polarization of tumour-associated macrophages to enhance cancer immunotherapy. *Nat. Biomed. Eng.* **2**, 578–588 (2018).
57. Loeuillard, E. *et al.* Targeting tumor-associated macrophages and granulocytic myeloid-derived suppressor cells augments PD-1 blockade in cholangiocarcinoma. *J. Clin. Invest.* **130**, 5380–5396 (2020).
58. Choo, Y. W. *et al.* M1 Macrophage-Derived Nanovesicles Potentiate the Anticancer Efficacy of Immune Checkpoint Inhibitors. *ACS Nano* **12**, 8977–8993 (2018).
59. Arlauckas, S. P. *et al.* Arg1 expression defines immunosuppressive subsets of tumor-associated macrophages. *Theranostics* **8**, 5842–5854 (2018).
60. Landry, A. P., Balas, M., Alli, S., Spears, J. & Zador, Z. Distinct regional ontogeny and activation of tumor associated macrophages in human glioblastoma. *Sci. Rep.* **10**, 19542 (2020).
61. Zheng, X. *et al.* Spatial Density and Distribution of Tumor-Associated Macrophages Predict Survival in Non-Small Cell Lung Carcinoma. *Cancer Res.* **80**, 4414–4425 (2020).
62. Etzerodt, A. *et al.* Specific targeting of CD163 + TAMs mobilizes inflammatory monocytes and promotes T cell-mediated tumor regression. *J. Exp. Med.* **216**, 2394–2411 (2019).

63. Puig-Kröger, A. *et al.* Folate Receptor  $\beta$  Is Expressed by Tumor-Associated Macrophages and Constitutes a Marker for M2 Anti-inflammatory/Regulatory Macrophages. *Cancer Res.* **69**, 9395–9403 (2009).
64. Viitala, M. *et al.* Immunotherapeutic Blockade of Macrophage Clever-1 Reactivates the CD8<sup>+</sup> T-cell Response against Immunosuppressive Tumors. *Clin. Cancer Res.* **25**, 3289–3303 (2019).
65. Linde, N. *et al.* Macrophages orchestrate breast cancer early dissemination and metastasis. *Nat. Commun.* **9**, 1–14 (2018).
66. Witschen, P. M. *et al.* Tumor Cell Associated Hyaluronan-CD44 Signaling Promotes Pro-Tumor Inflammation in Breast Cancer. *Cancers* **12**, 1325 (2020).
67. Guo, C. *et al.* Liposomal Nanoparticles Carrying anti-IL6R Antibody to the Tumour Microenvironment Inhibit Metastasis in Two Molecular Subtypes of Breast Cancer Mouse Models. *Theranostics* **7**, 775–788 (2017).
68. Movahedi, K. *et al.* Nanobody-Based Targeting of the Macrophage Mannose Receptor for Effective *In Vivo* Imaging of Tumor-Associated Macrophages. *Cancer Res.* **72**, 4165–4177 (2012).
69. Azad, A. K. *et al.*  $\gamma$ -Tilmanocept, a New Radiopharmaceutical Tracer for Cancer Sentinel Lymph Nodes, Binds to the Mannose Receptor (CD206). *J. Immunol.* **195**, 2019–2029 (2015).
70. Jameson, B. *et al.* Expression of DC-SIGN by Dendritic Cells of Intestinal and Genital Mucosae in Humans and Rhesus Macaques. *J. Virol.* **76**, 1866–1875 (2002).
71. Conriot, J. *et al.* Immunization with mannosylated nanovaccines and inhibition of the immune-suppressing microenvironment sensitizes melanoma to immune checkpoint modulators. *Nat. Nanotechnol.* **14**, 891–901 (2019).
72. Jaynes, J. M., Lopez, H. W., Martin, G. R., YATES, C. & Garvin, C. E. Peptides having anti-inflammatory properties. (2016).
73. Scodeller, P. & Ascitto, E. K. Targeting Tumors Using Peptides. *Molecules* **25**, 808 (2020).
74. Ekladius, I., Colson, Y. L. & Grinstaff, M. W. Polymer–drug conjugate therapeutics: advances, insights and prospects. *Nat. Rev. Drug Discov.* **18**, 273–294 (2019).
75. Duro-Castano, A., Conejos-Sánchez, I. & Vicent, M. J. Peptide-Based Polymer Therapeutics. *Polymers* **6**, 515–551 (2014).
76. Moura, L. I. F. *et al.* Functionalized branched polymers: promising immunomodulatory tools for the treatment of cancer and immune disorders. *Mater. Horiz.* **6**, 1956–1973 (2019).
77. Melnyk, T., Đorđević, S., Conejos-Sánchez, I. & Vicent, M. J. Therapeutic potential of polypeptide-based conjugates: Rational design and analytical tools that can boost clinical translation. *Adv. Drug Deliv. Rev.* **160**, 136–169 (2020).
78. Duro-Castano, A. *et al.* Capturing “Extraordinary” Soft-Assembled Charge-Like Polypeptides as a Strategy for Nanocarrier Design. *Adv. Mater.* **29**, 1702888 (2017).
79. Duro-Castano, A. *et al.* Well-Defined Star-Shaped Polyglutamates with Improved Pharmacokinetic Profiles As Excellent Candidates for Biomedical Applications. *Mol. Pharm.* **12**, 3639–3649 (2015).

80. Duro-Castano, A., Movellan, J. & Vicent, M. J. Smart branched polymer drug conjugates as nano-sized drug delivery systems. *Biomater. Sci.* **3**, 1321–1334 (2015).
81. Cortez-Retamozo, V. *et al.* Origins of tumor-associated macrophages and neutrophils. *Proc. Natl. Acad. Sci.* **109**, 2491–2496 (2012).
82. Kurashige, M. *et al.* Origin of cancer-associated fibroblasts and tumor-associated macrophages in humans after sex-mismatched bone marrow transplantation. *Commun. Biol.* **1**, 1–13 (2018).
83. Veglia, F. & Gabrilovich, D. I. Dendritic cells in cancer: the role revisited. *Curr. Opin. Immunol.* **45**, 43–51 (2017).
84. Agostinis, P. *et al.* PHOTODYNAMIC THERAPY OF CANCER: AN UPDATE. *CA. Cancer J. Clin.* **61**, 250–281 (2011).
85. Cheah, H. Y. *et al.* Near-Infrared Activatable Phthalocyanine–Poly-L-Glutamic Acid Conjugate: Enhanced in Vivo Safety and Antitumor Efficacy toward an Effective Photodynamic Cancer Therapy. *Mol. Pharm.* **15**, 2594–2605 (2018).
86. Nguyen, V.-N., Yan, Y., Zhao, J. & Yoon, J. Heavy-Atom-Free Photosensitizers: From Molecular Design to Applications in the Photodynamic Therapy of Cancer. *Acc. Chem. Res.* **54**, 207–220 (2021).
87. Tacar, O., Sriamornsak, P. & Dass, C. R. Doxorubicin: an update on anticancer molecular action, toxicity and novel drug delivery systems. *J. Pharm. Pharmacol.* **65**, 157–170 (2013).
88. Zhang, F. *et al.* Reprogramming of profibrotic macrophages for treatment of bleomycin-induced pulmonary fibrosis. *EMBO Mol. Med.* **12**, e12034 (2020).
89. Sartor, O. *et al.* Lutetium-177–PSMA-617 for Metastatic Castration-Resistant Prostate Cancer. *N. Engl. J. Med.* **0**, null (2021).
90. Vikas, P., Borchering, N. & Zhang, W. The clinical promise of immunotherapy in triple-negative breast cancer. *Cancer Manag. Res.* **10**, 6823–6833 (2018).
91. Tian, C. *et al.* ff19SB: Amino-Acid-Specific Protein Backbone Parameters Trained against Quantum Mechanics Energy Surfaces in Solution. *J. Chem. Theory Comput.* **16**, 528–552 (2020).
92. Case, D. A. *et al.* AMBER 2020 University of California, San Francisco (2020) <https://sbgrid.org/software/titles/ambertools>.
93. Hopkins, C. W., Le Grand, S., Walker, R. C. & Roitberg, A. E. Long-Time-Step Molecular Dynamics through Hydrogen Mass Repartitioning. *J. Chem. Theory Comput.* **11**, 1864–1874 (2015).
94. Berendsen, H. J. C., Postma, J. P. M., van Gunsteren, W. F., DiNola, A. & Haak, J. R. Molecular dynamics with coupling to an external bath. *J. Chem. Phys.* **81**, 3684–3690 (1984).
95. Ryckaert, J.-P., Ciccotti, G. & Berendsen, H. J. C. Numerical integration of the cartesian equations of motion of a system with constraints: molecular dynamics of n-alkanes. *J. Comput. Phys.* **23**, 327–341 (1977).
96. Ray, A. & Dittel, B. N. Isolation of Mouse Peritoneal Cavity Cells. *J. Vis. Exp. JoVE* 1488 (2010) doi:10.3791/1488.

## Figures

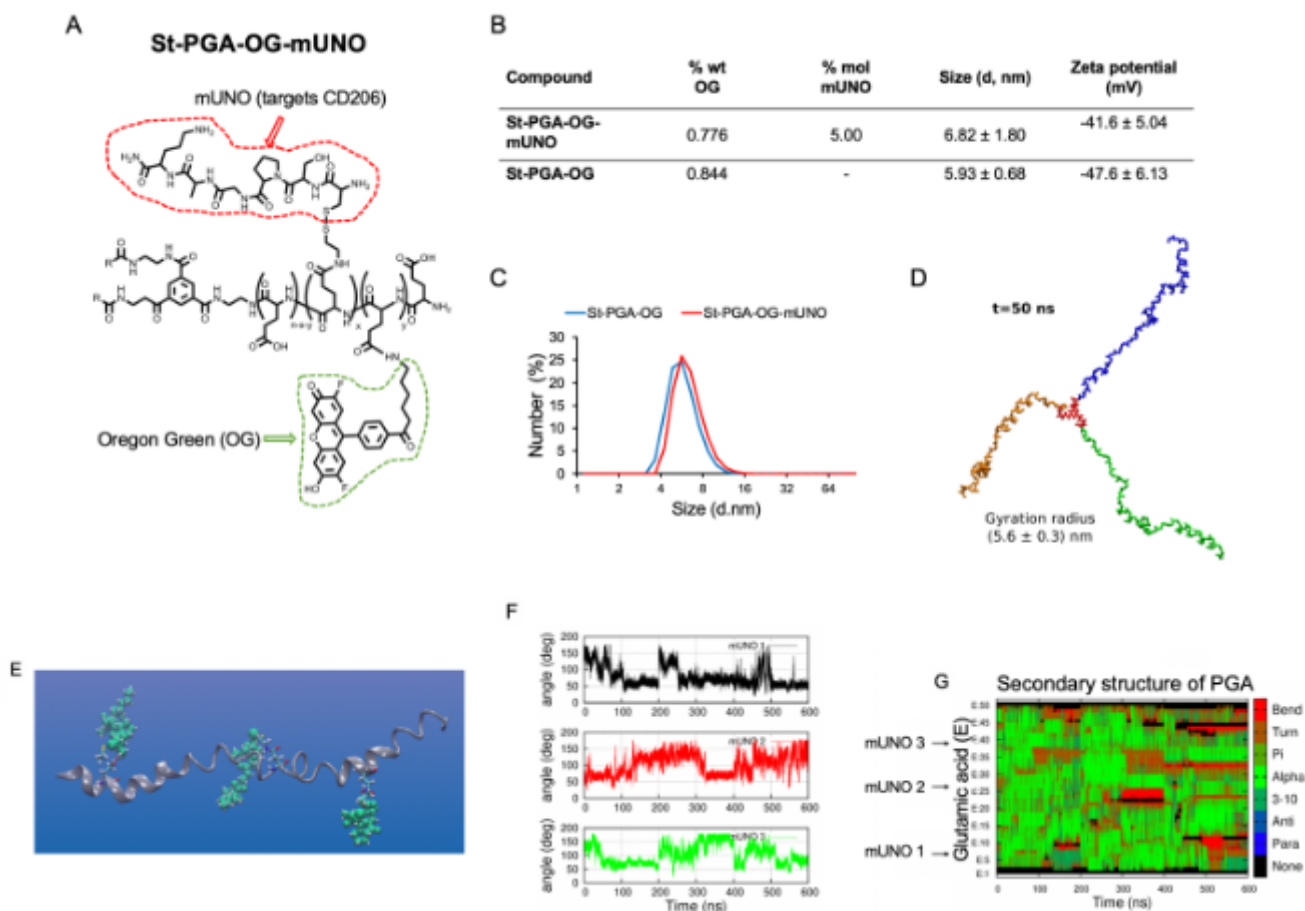


**Figure 1**

Design and analysis of mUNO-targeted St-PGA. (A) Representative structure of St-PGA decorated with mUNO peptides (red colour) and OG (green colour). (B) Table detailing OG loading, mUNO loading, size measured with DLS, and a charge measured with Zeta potential analysis. (C) DLS graph demonstrating uniform nanoconjugate size for both St-PGA-OG-mUNO and St-PGA-OG. (D) A snapshot of modelled St-PGA structure in water and Na<sup>+</sup> counterions at the last stage of the simulation (50 ns), displays the three arms are in different colours for visual clarity. The average gyration radius was 5.6 ± 0.3nm, t shows time in ns. (E) Representative MD snapshot of a single St-PGA-mUNO branch containing three equidistant mUNO peptides. Green spheres represent mUNO and the linker is represented using Licorice representation. (F) mUNO rotation around the PGA chain for each of the three peptides (black, red, and magenta lines). (G) PGA chain secondary structure evolution, where red and brown regions show how mUNO perturbs the chain structure, turning alpha helices into random coils.

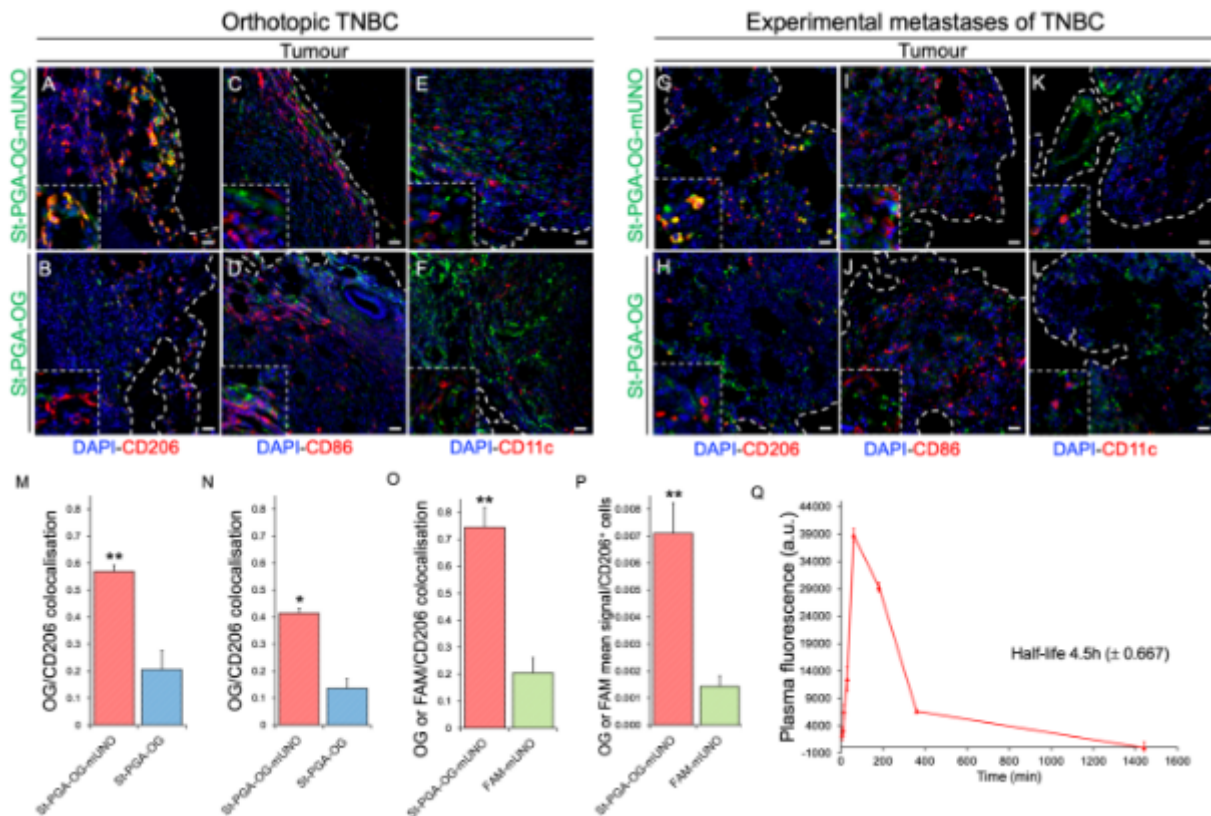


**Figure 2**

St-PGA-OG-mUNO targets CD206+ TAMs in the orthotopic and experimental metastases of TNBC and displays an extended plasma half-life. Homing studies with i.p. administered St-PGA-OG-mUNO (0.41 mg/0.5mL of PBS) or St-PGA-OG (0.35 mg/0.5mL of PBS), after a 6 h circulation. N=3 for the orthotopic TNBC and N=2 for the experimental metastases of TNBC. (A-F) Homing in the orthotopic TNBC. (A) St-PGA-OG-mUNO displayed high colocalisation between OG and CD206 (yellow signal), whereas (B) St-PGA-OG displayed minimal colocalisation. St-PGA-OG-mUNO and St-PGA-OG did not show any homing to CD86+ cells (M1 macrophages) (C, D) nor CD11c+ cells (DCs) (E, F). (G-L) Homing study in the experimental metastases of TNBC. (G) St-PGA-OG-mUNO displayed high colocalisation with OG and CD206 (yellow signal), whereas (H) St-PGA-OG showed minimal colocalisation. St-PGA-OG-mUNO and St-PGA-OG did not show any homing to CD86+ cells (M1 macrophages) (I, J) or CD11c+ cells (DCs) (K, L). Scale bars represent 20  $\mu$ m. (M) Graph depicting the quantification of CD206 and OG colocalisation in the orthotopic TNBC and (N) the experimental metastases of TNBC. (O) Quantification of colocalisation analysis for St-PGA-OG-mUNO or FAM-mUNO with CD206 homing after 6 h of circulation, N=2 (30nmoles in OG and FAM, respectively). Colocalisation was quantified using Fiji programme and Pearson's coefficient (for more information see Materials and methods). (P) Mean OG/FAM signal per CD206+ cell analysed using the ImageJ programme. (Q) Plasma fluorescence (in the green channel) of i.p. administered St-PGA-OG-mUNO (dose 15nmoles in OG) in healthy Balb/c mice (N=3). Error bars represent standard error (SE).

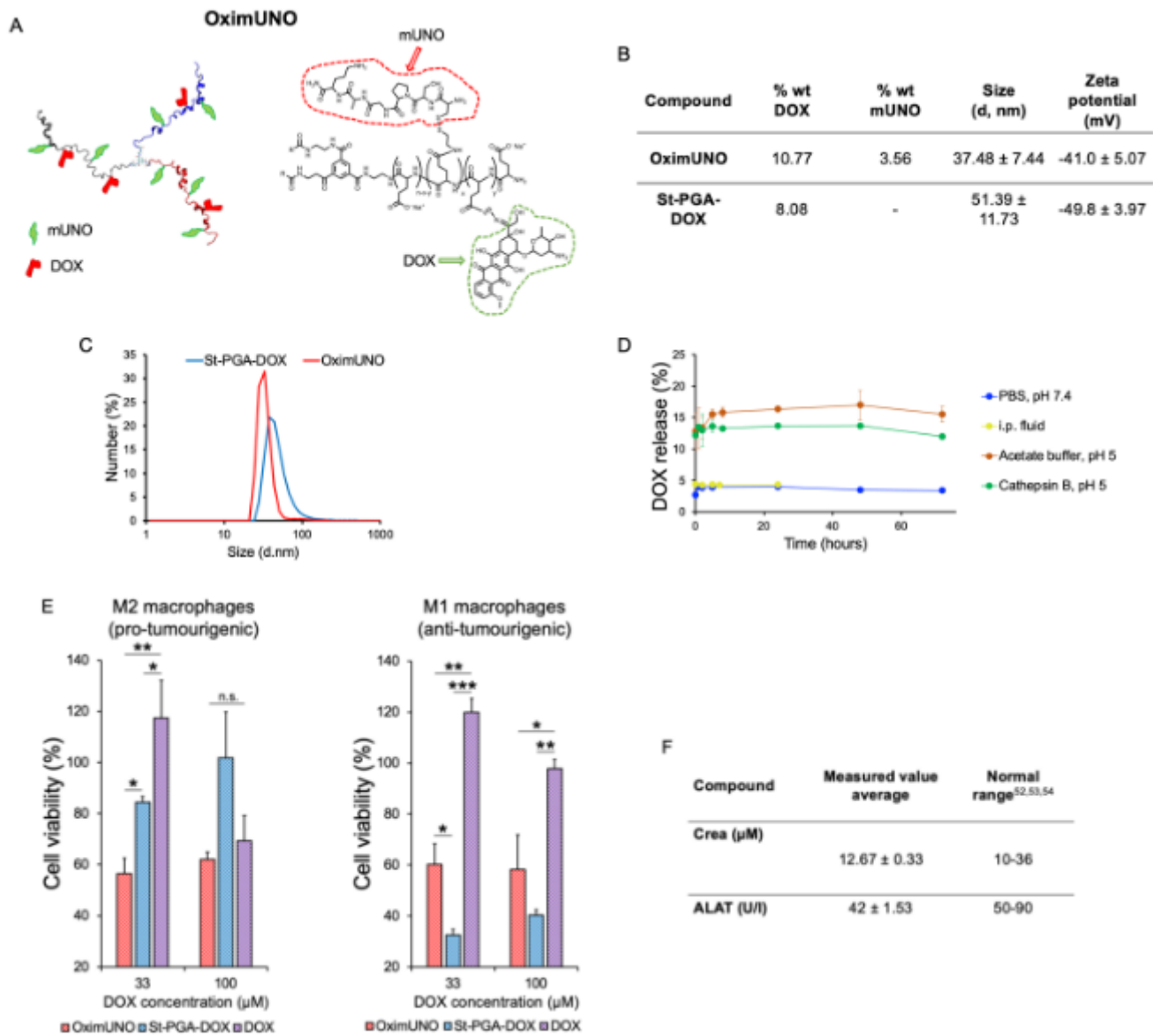


**Figure 3**

OximUNO enhances the in vitro efficacy of DOX on M2 macrophages in vitro. (A) Simplified form of OximUNO (left) and molecular structure (right) showing St-PGA decorated with mUNO (red) and DOX (green). (B) Table showing DOX loading, mUNO loading, size measured with DLS, and charge measured with Zeta potential of both nanoconjugates in PBS. (C) A DLS graph for measurements in (B) showing uniform size of OximUNO and St-PGA-DOX. (D) DOX release from OximUNO showing the drug release in PBS, i.p. fluid, acetate buffer or cathepsin B. (E) In vitro cytotoxicity on primary human M2 (left panel) or M1 (right panel) macrophages of OximUNO (red bars), St-PGA-DOX (blue bars), and DOX (purple bars) following a 15 min incubation, washed, cultured for additional 48 h, and then analysed for cell viability using MTT assay. (F) Liver and kidney toxicology serum levels of Crea and ALAT following i.p.-administration of OximUNO in healthy Balb/c mice (N=3). Error bars represent SE.

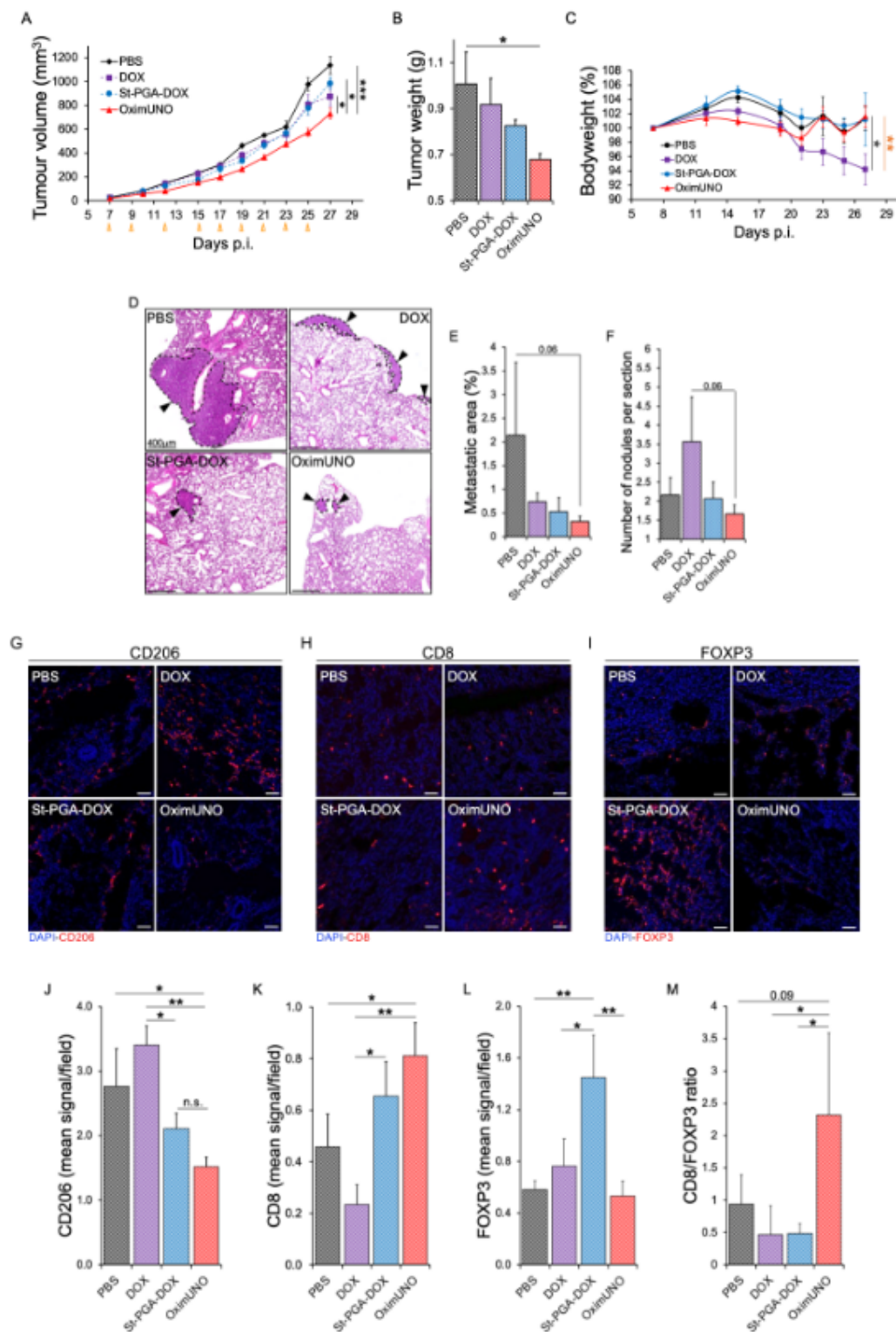


**Figure 4**

OximUNO monotherapy reduces primary tumour growth, pulmonary metastases, and alleviates immunosuppression. Monotherapy with OximUNO, St-PGA-DOX, or DOX at 2 mg/kg of DOX in mice bearing orthotopic TNBC tumours (N=5). I.p. injections began when tumours reached 25 mm<sup>3</sup> and were performed every other day, to give a total of nine injections. (A) Tumour volumes shown at the end of treatment study. Orange arrows indicate injection days. (B) Primary tumour weights at the end of the

treatment, demonstrating significantly smaller weights for OximUNO-treated mice (red bar) compared to other groups. (C) Mouse bodyweight analysis demonstrating that OximUNO did not negatively impact bodyweight (red line); meanwhile DOX-treatment induced significant reduction in bodyweight at the end of the treatment (purple line). Dark grey \* DOX vs. PBS, orange \* DOX vs. St-PGA-DOX. (D) Representative H&E images showing pulmonary metastases for all groups (scale bars represent 400  $\mu\text{m}$ ); OximUNO treatment induced the smallest metastatic area (E) and the lowest number of average nodules per lung (F). (G-I) Representative confocal microscopy images demonstrating the expression of (G) CD206, (H) CD8, and (I) FOXP3. Scale bars represent 50  $\mu\text{m}$ . (J-M) Quantification of confocal microscopy images for expression of (J) CD206, (K) CD8, and (L) FOXP3. (M) Graph of CD8/FOXP3 expression ratio showing a shift in the immune profile. Quantification was performed using the ImageJ programme from at least three images per mouse and five mice per group. Error bars represent SE.

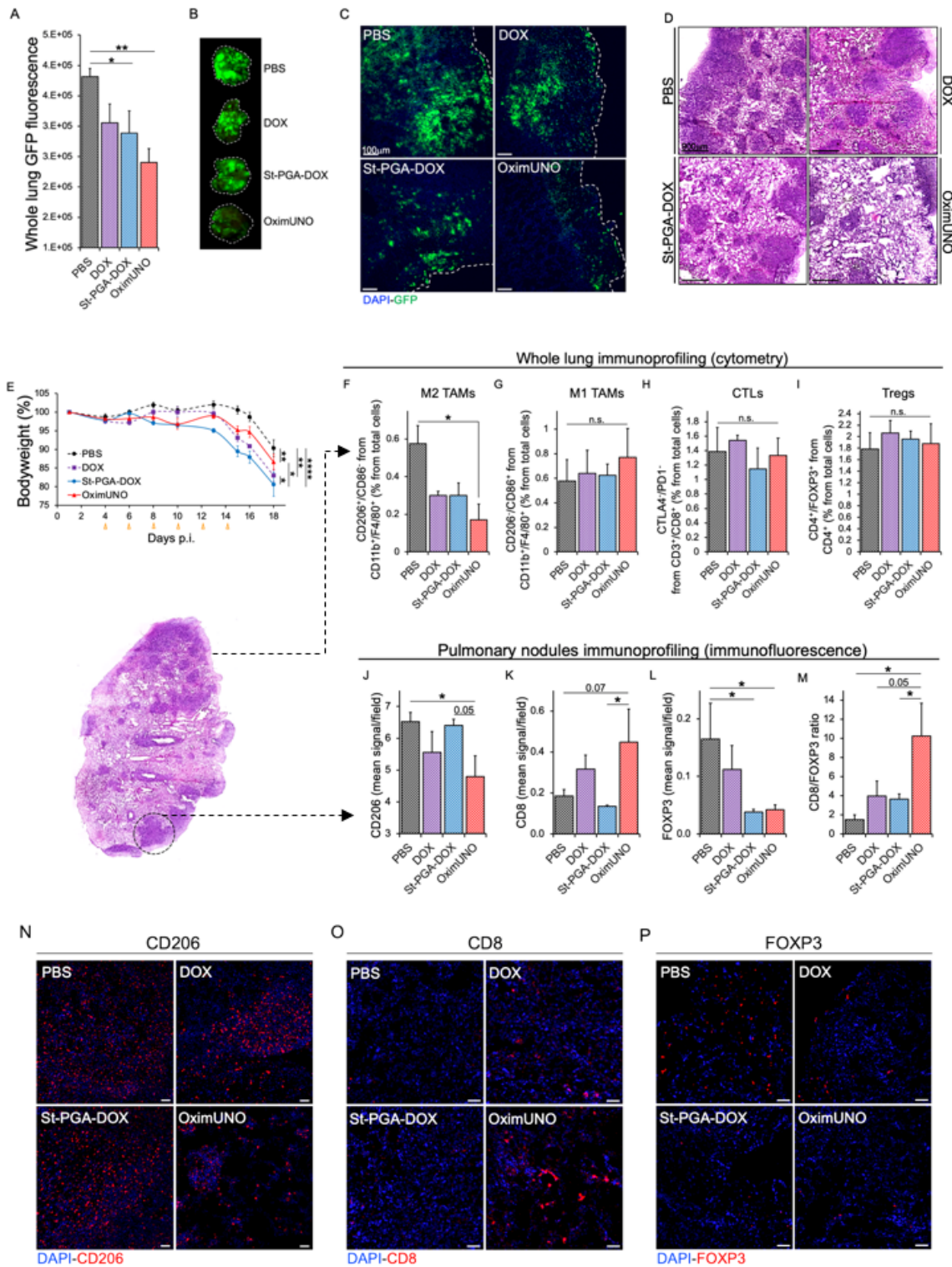


**Figure 5**

OximUNO monotherapy in the experimental metastases of TNBC significantly reduces tumour burden, CD206<sup>+</sup> TAMs and alleviates immunosuppression. Monotherapy with OximUNO, St-PGA-DOX, or DOX at 2mg/kg of DOX in the experimental metastases of TNBC, created using GFP-labelled 4T1 cells (N=6). I.p. injections began on day four p.i. and were performed every other day to give a total of six injections. (A) Quantification of whole lung GFP fluorescence at the end of the treatment using the ImageJ programme

(N=6). (B) Representative macroscopic photographs of GFP fluorescence in lungs. (C) Representative confocal microscopy images of GFP expression, scale bars represent 100  $\mu\text{m}$ . (D) Representative H&E images showing pulmonary metastases for all groups (scale bars represent 900  $\mu\text{m}$ ). (E) Mouse bodyweights, demonstrating that OximUNO had a small effect on bodyweight (red line) whereas St-PGA-DOX-treated mice started to lose weight from day eight p.i. and DOX-treated mice from day 15 p.i. Orange arrows indicate injection days. (F-I) FC analysis on three right lungs per group. (F) M2 TAMs (CD206+), (G) M1 TAMs, (H) CTLs and (I) Tregs. (J-M) IF analysis on the tumour nodules to detect the expression of different markers: (J) CD206, (K) CD8, (L) FOXP3. (M) Graph showing CD8/FOXP3 ratio. Quantification of IF images was carried out using the ImageJ programme from at least five images per mouse and three mice per group. (N-P) Representative confocal microscopy images for (N) CD206, (O) CD8, and (P) FOXP3. Scale bars represent 50  $\mu\text{m}$ . Error bars represent SE.

## Supplementary Files

This is a list of supplementary files associated with this preprint. Click to download.

- [OximUNOsupplementaryinformation.pdf](#)
- [VideoS1.gif](#)